J. Fluid Mech. (1995), *vol.* 305, *pp.* 307–345

Inviscid separated flow over a non-slender delta wing

By D. W. MOORE[1] AND D. I. PULLIN[2]

[1]Department of Mathematics, Imperial College of Science, Technology and Medicine, Queens Gate London SW7 2BZ, UK

[2]Graduate Aeronautical Laboratories 105-50, California Institute of Technology, Pasadena, CA 91125, USA

(Received 16 May 1995 and in revised form 29 August 1995)

We consider inviscid incompressible flow about an infinite non-slender flat delta wing with leading-edge separation modelled by symmetrical conical vortex sheets. A similarity solution for the three-dimensional steady velocity potential Φ is sought with boundary conditions to be satisfied on the line which is the intersection of the wing–sheet surface with the surface of the unit sphere. A numerical approach is developed based on the construction of a special boundary element or 'winglet' which is effectively a Green function for the projection of $\nabla^2\Phi = 0$ onto the spherical surface under the similarity ansatz. When the wing semi-apex angle γ_0 is fixed, satisfaction of the boundary conditions of zero normal velocity on the wing and zero normal velocity and pressure continuity across the vortex sheet then leads to a nonlinear eigenvalue problem. A method of ensuring a condition of zero lateral force on a lumped model of the inner part of the rolled-up vortex sheet gives a closed set of equations which is solved numerically by Newton's method. We present and discuss the properties of solutions for γ_0 in the range $1.3^\circ \leqslant \gamma_0 \leqslant 89.5^\circ$. The dependencies of these solutions on γ_0 differs qualitatively from predictions of slender-body theory. In particular the velocity field is in general not conical and the similarity exponent must be calculated as part of the global eigenvalue problem. This exponent, together with the detailed flow field including the position and structure of the separated vortex sheet, depend only on γ_0. In the limit of small γ_0, a comparison with slender-body theory is made on the basis of an effective angle of incidence.

1. Introduction

1.1. *Flow past a symmetric delta wing at incidence*

Despite the availability of powerful computers, the calculation of the incompressible flow past a wing in three dimensions remains a challenge. Even if we ignore the presence of turbulent boundary layers and the turbulent wake and regard the flow as laminar, severe difficulties arise because of the need to resolve the shear layers separating from the wing surface.

A strategy for bypassing this difficulty is to regard the flow as inviscid and to replace the shear layers by vortex sheets. Of course, the problem of determining the location of the separation cannot be solved within the framework of inviscid theory. However, wings have highly curved edges and it is plausible to regard these edges

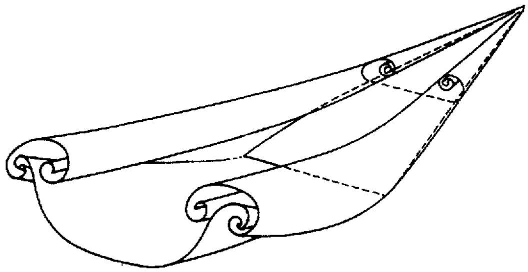

FIGURE 1. Inviscid model of vortex-sheet separation from a delta wing at incidence in a uniform stream. From Kuchemann (1975). On the forward portion of the wing the vortex-sheet shape is nearly conical.

as candidates for separation lines. Whether a particular edge experiences separation or not must be decided ultimately by comparison with experiment. For example, a slender delta wing experiences leading-edge separation only at higher angles of incidence – the critical incidence being determined only by experiment – whereas the trailing edge always sheds a vortex sheet. Another complication is the occurrence of 'secondary' separations from the smooth surfaces of the wing, whose location cannot be determined on the basis of inviscid theory (see Thompson 1975; Kirkkopru & Riley 1991, and the references cited there). Figure 1 sketches an example of the inviscid model, with vortex sheets separating from all three edges of a delta wing, taken from Kuchemann (1975).

This inviscid strategy has been powerfully advocated by Kuchemann and was – in part – implemented in a series of papers emanating from the Royal Aircraft Establishment in the period 1960–1980. In particular, Smith (1968) was able to calculate, for the first time, the position of the leading-edge vortices produced by a slender delta wing and to calculate the extra lift produced; good agreement with wind-tunnel measurements was obtained.

Smith deployed slender-body theory to simplify the calculation. In this theory, the delta wing is taken to be infinitely long so that the trailing edge is not allowed to affect the flow. The governing equations are simplified by retaining only cross-flow derivatives and – while the problem remains nonlinear – the calculation is effectively two-dimensional although the boundary conditions contain the conical character of the three-dimensional flow.

1.2. *The non-slender delta wing*

We wish to remove the restriction of slenderness while – to make the problem tractable – we retain the assumption that the wing is semi-infinite, so that trailing-edge effects are negligible. We begin by introducing Cartesian coordinates (x, y, z) with corresponding unit vectors $(\boldsymbol{i}, \boldsymbol{j}, \boldsymbol{k})$ and consider a wing of zero thickness in the plane $z = 0$ whose edges are $y = \pm x \tan \gamma_0$, where γ_0 is the semi-apex angle of the wing. The wing thus occupies the region $-x \tan \gamma_0 \leqslant y \leqslant x \tan \gamma_0$ in the plane $z = 0$.

In order to see the nature of the problem we are to attack, it is helpful to examine the simpler problem of determining the attached flow. Thus, we seek a harmonic potential $\phi(x, y, z)$ which has zero normal derivative on the wing, vanishes off the wing in the plane $z = 0$ and is allowed to be singular at the edges $y = \pm x \tan \gamma_0$; precisely, the speed $|\nabla \phi|$ is allowed to behave like $d^{-1/2}$, where d is the distance of a field point from the nearest point on an edge.

To proceed, we introduce spherical polar coordinates (R, θ, ψ) defined by

$$\left.\begin{array}{rcl} x &=& R\cos\theta, \\ y &=& R\sin\theta\cos\psi, \\ z &=& R\sin\theta\sin\psi, \end{array}\right\} \tag{1.1}$$

We seek a similarity solution by writing

$$\phi(R,\theta,\psi) = R^n\,\Phi(\theta,\psi) \tag{1.2}$$

with velocity components

$$v_R = \frac{\partial\phi}{\partial R} = n R^{n-1}\,\Phi(\theta,\psi), \tag{1.3}$$

$$v_\theta = \frac{1}{R}\frac{\partial\phi}{\partial\theta} = R^{n-1}\frac{\partial\Phi}{\partial\theta}, \tag{1.4}$$

$$v_\psi = \frac{1}{R\,\sin\theta}\frac{\partial\phi}{\partial\psi} = R^{n-1}\frac{1}{\sin\theta}\frac{\partial\Phi}{\partial\psi}, \tag{1.5}$$

where n is the similarity index. The reduced potential Φ satisfies an equation which follows from substitution of (1.2) into the Laplace equation

$$\frac{1}{\sin\theta}\frac{\partial}{\partial\theta}\left(\sin\theta\frac{\partial\Phi}{\partial\theta}\right) + \frac{1}{\sin^2\theta}\frac{\partial^2\Phi}{\partial\psi^2} + n(n+1)\,\Phi = 0, \tag{1.6}$$

with boundary conditions

$$\frac{\partial\Phi}{\partial\psi} = 0 \quad \text{on} \quad 0 \leqslant \theta \leqslant \gamma_0, \quad \psi = 0, \tag{1.7}$$

$$\Phi = 0 \quad \text{on} \quad \gamma_0 \leqslant \theta \leqslant \pi, \tag{1.8}$$

and the symmetry requirement†

$$\Phi(\theta,\psi) = \Phi(\theta,\pi-\psi)\,; \tag{1.9}$$

the singularity at $\theta = \gamma_0$, $\psi = 0$ being as specified.

1.3. *The attached flow*

This problem was solved by Brown & Stewartson (1969, henceforth referred to as BS), who showed that n depended on γ_0 and that as γ_0 increased from zero to $\pi/2$, $n(\gamma_0)$ decreased monotonically from 1 to $\frac{1}{2}$. Moreover, for $\gamma_0 \ll 1$ they showed that

$$n(\gamma_0) = 1 - \tfrac{1}{4}\gamma_0^2 + \tfrac{1}{8}\gamma_0^4\log\gamma_0 + \cdots. \tag{1.10}$$

We note some features of this attached flow solution.

(*a*) Since $n < 1$ for $\gamma_0 > 0$, the velocity field $\nabla\phi$ tends to zero as $R \to \infty$. Thus we *cannot* match this solution to a uniform stream at infinity. The BS solution is an eigenfunction. The magnitude of the eigenfunction cannot be determined unless the flow past a finite delta wing is calculated. As long as attached flow is assumed, the BS solution will hold near the apex of a finite delta wing, whatever the angle of incidence. But if the angle of incidence is small, so that lifting-surface theory can be used, the region in which the BS solution dominates the flow can be estimated (Sells unpublished – see Riley & Smith 1985).

(*b*) The passage to the slender-body limit is non-uniform. The speed q behaves like $R^{-\gamma_0^2/4}$, so that, at fixed R, slender-body theory is achieved as $\gamma_0 \to 0$ whereas at fixed

---

† We do not discuss the possibility of other solutions.

γ_0, however small, $q \to \infty$ as $R \to 0$, violating the assumption of slender-body theory. Mathematically, we have

$$\lim_{R\to 0}\lim_{\gamma_0\to 0} R^{n-1}\nabla\Phi(\theta,\psi,\gamma_0) \neq \lim_{\gamma_0\to 0}\lim_{R\to 0} R^{n-1}\nabla\Phi(\theta,\psi,\gamma_0). \qquad (1.11)$$

(*c*) The solution ceases to be an eigenfunction when $n = 1$, but then has a constant velocity field at infinity. In this case – and in this case only – a uniform flow of arbitrary strength in the plane of the wing can be added to the attached solution so that the resulting composite velocity field reduces to an incident uniform velocity field at infinity.

1.4. *Separated flow*

Our objective is to calculate the separated analogue of the BS attached solution. We will again assume the form (1.2) and augment the boundary conditions (1.6), (1.7), and (1.8) by requiring zero normal velocity on and continuity of pressure across conical vortex sheets springing from the wing edges. The location of the vortex sheets is unknown as is the similarity parameter n – and we have to verify that $n(\gamma_0) < 1$, so that our separated flow is an eigenfunction. The similarity parameter n is determined by both the linear kinematic requirement of zero normal velocity on the wing and the nonlinear dynamic boundary conditions on the vortex sheets. The determination of the similarity parameter is unusual, but not unprecedented and a well-known example is Guderly's (1942) solution for a contracting spherical shock wave. Although the vortex sheets are conical in shape – indeed there is no other possibility given that we are seeking a steady flow solution for which no length scale is provided by either the equations of motion or by the boundary conditions – the flow itself is non-conical in the usual sense (that is, the velocity is not constant on rays originating from the apex), except where $n = 1$.

If such a solution exists, then it follows that the structure of flow near the apex of a finite delta wing will be independent of the true angle of incidence. In particular, the position – but not the strength – of the vortex sheets can depend only on γ_0. The strength of the sheets will be determined only when the separated-flow eigenfunction emerges as the local form of the global solution for a finite delta wing.

We have chosen to solve the problem by use of a vortex method. This is a little more difficult than in two dimensions. Although the transformation (1.2) projects the velocity potential onto the unit sphere, the vorticity is *not* normal to the surface of the sphere and the analogy with plane flow is lost. We cannot generate the projected potential by placing an array of point vortices on the wing and sheet – indeed, an isolated line vortex emerging from the apex cannot exist. This is because its circulation would have to depend on distance from the apex like R^n, violating Kelvin's circulation theorem.

In §2, we tackle this problem and devise an element – which we call a winglet – which is analogous to the familiar horseshoe vortex of lifting-surface theory. It emerges that its potential can be expressed in terms of hypergeometric functions and we describe an effective method of computing these in §6.

The boundary integrals turn out to be Hadamard principal parts and we show how to calculate these in §3 where – as a check on our formulation – we reconsider the BS problem. Excellent agreement for n obtained by our method and n obtained from the BS method is found.

In §§4 and 5, we give some details of our formulation. In particular, we tackle the

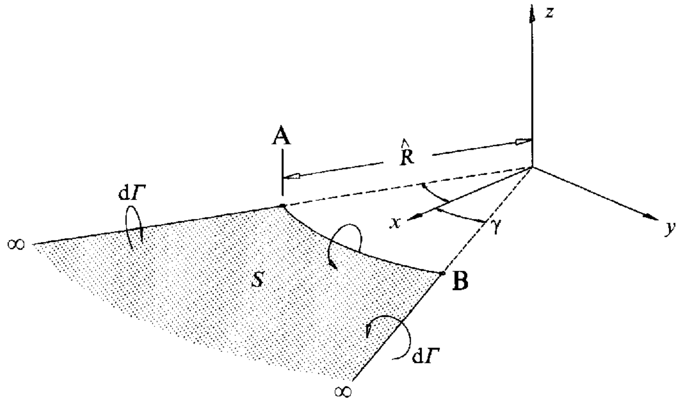

FIGURE 2. Construction of the elementary horseshoe vortex ∞AB∞.

problems of describing the spiral part of the vortex sheet and of ensuring that the vortex sheet separates from the wing tip so as to avoid large adverse pressure gradients.

In §6, we give details of two numerical methods while in §7 we describe our results and discuss their accuracy. We pay particular attention to certain properties the solution must possess, because these enable us to estimate the accuracy of our work.

2. Construction of the boundary element

2.1. *The winglet potential*

We decided to take as our starting point an elementary horseshoe vortex modified to fit our geometry. We thus form a vortex line $L_{\hat{R}}$ lying in the plane $z = 0$, consisting of the half-line $\hat{\theta} = -\gamma$, $\infty > \hat{r} \geqslant \hat{R}$, the circular arc $\hat{r} = \hat{R}$, $-\gamma \leqslant \hat{\theta} \leqslant \gamma$ and the half-line $\hat{\theta} = \gamma$, $\hat{R} \leqslant \hat{r} < \infty$ where we use polar coordinates ($\hat{r}$, $\hat{\theta}$) in the plane $z = 0$ (figure 2). The self-induced velocity of $L_{\hat{R}}$ is infinite on the curved portion, but this singularity disappears in the integration. The winglet has infinite self-induced velocity at points along its edges and thus resembles the straight elements of uniform strength sometimes used to represent a vortex sheet in plane flow. We examined the possibility of extending the treatment given by Van der Vooren (1980) but the resulting formulae are very cumbersome. We assume the vortex line has circulation dΓ relative to a sense of description in which the line $\hat{\theta} = -\gamma$ is described in the $\hat{r}$-decreasing direction. The velocity potential $\mathrm{d}\phi(\boldsymbol{x};R)$ ($\boldsymbol{x} = (x, y, z)$ as in (1.1)) due to the vortex line $L_{\hat{R}}$ is

$$\mathrm{d}\phi\left(\boldsymbol{x};\hat{R}\right) = \frac{\mathrm{d}\Gamma}{4\pi}\iint_{S} \frac{(\boldsymbol{x}-\hat{\boldsymbol{x}})\cdot\hat{\boldsymbol{k}}}{\Delta^3}\,\hat{r}\,\mathrm{d}\hat{r}\,\mathrm{d}\hat{\theta}, \tag{2.1}$$

where S is the plane surface spanning the vortex line, $\hat{\boldsymbol{x}} = (\hat{r}\cos\hat{\theta}, \hat{r}\sin\hat{\theta}, 0)$,

$$\Delta^2 = \left(\hat{r}\cos\hat{\theta} - R\cos\theta\right)^2 + \left(\hat{r}\sin\hat{\theta} - R\sin\theta\cos\psi\right)^2 + R^2\sin^2\theta\sin^2\psi, \tag{2.2}$$

and where the field point $\boldsymbol{x}$ is expressed in spherical polars. Hence

$$\mathrm{d}\phi\left(\boldsymbol{x};\hat{R}\right) = \frac{\mathrm{d}\Gamma z}{4\pi}\int_{\hat{R}}^{\infty}\int_{-\gamma}^{\gamma}\frac{\hat{r}\,\mathrm{d}\hat{r}\,\mathrm{d}\hat{\theta}}{\Delta^3}. \tag{2.3}$$

We now consider the potential of a continuous distribution of vortex lines $L_{\hat{R}}$ occupying the range $0 \leqslant \hat{R} < \infty$. In order to conform to the overall similarity we must take

$$\mathrm{d}\Gamma = n B_0 \hat{R}^{n-1}\, \mathrm{d}\hat{R}, \tag{2.4}$$

where B_0 is a dimensional strength constant. The net velocity potential $\phi(\boldsymbol{x})$ is then given by

$$\phi(\boldsymbol{x}) = \frac{n B_0 z}{4\pi} \int_0^{\infty} \hat{R}^{n-1} \int_{\hat{R}}^{\infty} \int_{-\gamma}^{\gamma} \frac{\mathrm{d}\hat{R}\, \hat{r}\, \mathrm{d}\hat{r}\, \mathrm{d}\hat{\theta}}{\varDelta^3}. \tag{2.5}$$

If we invert the order of integration in $\hat{r}$ and $\hat{R}$ we find that the $\hat{R}$-integration can be performed, and we have

$$\phi(\boldsymbol{x}) = \frac{z B_0 R^{n-1}}{4\pi} \int_{-\gamma}^{\gamma} \mathrm{d}\hat{\theta} \left(\int_0^{\infty} \frac{s^{n+1}\, \mathrm{d}s}{\left(1 - 2s\cos\beta + s^2\right)^{3/2}} \right), \tag{2.6}$$

where

$$\cos\beta = \cos\theta\, \cos\hat{\theta} + \sin\theta\, \sin\hat{\theta}\, \cos\psi. \tag{2.7}$$

We recognize that β is the geodesic (or great circle) distance on the unit sphere between the field point $\boldsymbol{x}$ and the point $(\cos\hat{\theta}, \sin\hat{\theta}, 0)$ on the surface of the element.

The integral with respect to s can be evaluated (Magnus & Oberhettinger 1954, p. 68) and we find that, writing $\phi = R^n \varPhi$,

$$\varPhi = \frac{B_0\, n(n+1) \sin\theta \sin\psi}{4 \sin \pi n} \int_{-\gamma}^{\gamma} \frac{P_n^{-1}(-\cos\beta)}{\sin\beta} \mathrm{d}\hat{\theta}, \tag{2.8}$$

where P_n^{-1} is the associated Legendre function of degree -1 and order n and where the dependence of β on $\hat{\theta}$ is given in equation (2.7).

One property of (2.8) is worth noting here. From the fact that the velocity potential of the element is $-(\mathrm{d}\Gamma/4\pi)\Omega(\boldsymbol{x})$, where $\Omega(\boldsymbol{x})$ is the solid angle subtended by S at $\boldsymbol{x}$, we can see that the potential jumps by $\mathrm{d}\Gamma$ if we cross S in the z-increasing direction, while it is continuous off S. From this we can deduce that $\varPhi$ increases by B_0 as we cross the plane $z = 0$ in the z-increasing direction in the range $-\gamma < \hat{\theta} < \gamma$. From symmetry, it follows that $\varPhi \to \frac{1}{2}B_0$ as we approach the element from above and $\varPhi \to -\frac{1}{2}B_0$ as we approach the element from below. This can be verified analytically, by the method described below.

2.2. *The limit* $\gamma \to 0$

It is instructive to examine a limiting form of equation (2.8). Suppose we fix (θ, ψ) and let $\gamma \to 0$ and $B_0 \to \infty$ in such a way that $2\gamma B_0$ is finite and equal to B_1. We can set $\hat{\theta} = 0$ in (2.7) to find that $\beta = \theta$ and so

$$\varPhi \to B_1 P_n^{-1}(-\cos\theta) \sin\psi. \tag{2.9}$$

We can show that $\varPhi$ satisfies equation (1.3) and that $\varPhi$ is analytic except for $\theta = 0$. This last property is evident from the formula, easily derived from standard results (Magnus & Oberhettinger 1954, p. 60),

$$\Gamma(1+m) P_n^{-m}(-\cos\theta) = \left(\cot\theta/2\right)^m {}_2F_1\left(-n, n+1, m+1; \cos^2\theta/2\right). \tag{2.10}$$

The hypergeometric function is singular at $\theta = 0$, but the expansion in the neighbourhood at $\theta = 0$ can be deduced from results given by Abramowitz & Stegan (1964,

p. 559) and from (2.10), and we find that

$$P_n^{-1}(-\cos\theta) = \frac{c_0}{\theta} + \left(c_1 \log\left(\theta^2/4\right) + c_2\right)\theta + O\left(\theta^3 \log\theta^2\right) \tag{2.11}$$

where the constants c_0, c_1, and c_2 are given by

$$\left.\begin{aligned} c_0 &= \frac{2\sin\pi n}{n(n+1)\pi}, \quad c_1 = -c_0\, n(n+1)/4 \\ \text{and} \quad c_2 &= c_1\left(-1 + 2C + \operatorname{dig}(1-n) + \operatorname{dig}(2+n)\right) - c_0/12, \end{aligned}\right\} \tag{2.12}$$

where C is Euler's constant and dig is the digamma function. Thus, to leading order, (2.9) reduces to

$$\Phi = B_1 c_0 \frac{\sin\psi}{\theta}. \tag{2.13}$$

Now the geodesic distance from the origin to the point $(\theta,\ \psi)$ is θ, so we see that (2.13) is a vortex dipole, with its axis along $\psi = 0$.

The higher terms in (2.11) represent curvature effects. This is an important observation, because it means that the strongly singular part of the winglet potential Φ is a solution of Laplace's equation in the plane. We can thus appeal to standard results when we have to deal with the singular integrals which arise when we attempt to evaluate Φ and its derivatives on the wing, or sheets.

Before we face the complexities of applying these ideas to the separated flow, it is instructive to reconsider the attached flow problem of BS from our viewpoint. We attempt this in §3.

3. The attached-flow solution derived by a boundary integral technique

3.1. *The eigenvalue problem*

We represent the attached flow by a distribution of winglets. We thus write

$$\Phi(\theta,\psi) = A\sin\theta\sin\psi \int_{-\gamma_0}^{\gamma_0} \frac{P_n^{-1}(-\cos\beta)}{\sin\beta} f(\hat{\theta})\mathrm{d}\hat{\theta}, \tag{3.1}$$

where $A = B_0\, n(n+1)/(4\sin\pi n)$, where B_0 is defined in equation (2.8) and where $f(\hat{\theta})$ is the strength of the winglet distribution. This equation holds at points $(\theta,\ \psi)$ not on the wing.

We now reconsider the boundary value problem posed in equations (1.6)–(1.9). It is clear that $\Phi(\theta,0) = 0$ for $\theta > \gamma_0$, since $\beta > 0$ and the integrand is finite in this range of θ. The symmetry condition is satisfied if $f(\hat{\theta})$ is an even function. Thus it remains to satisfy the condition on $f(\hat{\theta}) \sim (\gamma_0 - \hat{\theta})^{1/2}$ as $\hat{\theta} \to \gamma_0$ and the condition of zero normal velocity (1.7).

We consider the limiting form of the ψ-component of the velocity as $(\theta,\psi) \to (\hat{\theta}_0, 0)$ where $0 \leqslant \hat{\theta}_0 < \gamma_0$. Now we can write

$$\Phi = A\sin\theta\sin\psi \left[\int_{-\gamma_0}^{\hat{\theta}_0-\varepsilon} + \int_{\hat{\theta}_0+\varepsilon}^{\gamma_0} + \int_{\hat{\theta}_0-\varepsilon}^{\hat{\theta}_0+\varepsilon}\right] f(\hat{\theta}) \frac{P_n^{-1}(-\cos\beta)}{\sin\beta}\,\mathrm{d}\hat{\theta}, \tag{3.2}$$

where ε is a small fixed constant. On differentiating this expression with respect to ψ we find that

$$\frac{1}{\sin\theta}\frac{\partial\Phi}{\partial\psi} = A\left(\int_{-\gamma_0}^{\hat{\theta}_0-\varepsilon} + \int_{\hat{\theta}_0+\varepsilon}^{\gamma_0}\right)\frac{f(\hat{\theta})P_n^{-1}\left(-\cos(\theta-\hat{\theta})\right)\,\mathrm{d}\hat{\theta}}{\sin(\theta-\hat{\theta})}$$
$$+A\frac{\partial}{\partial\psi}\left(\sin\psi\int_{\hat{\theta}_0-\varepsilon}^{\hat{\theta}_0+\varepsilon}\frac{f(\hat{\theta})P_n^{-1}(-\cos\beta)}{\sin\beta}\,\mathrm{d}\hat{\theta}\right), \qquad (3.3)$$

where we have taken the limit $\psi \to 0$ in the first two terms, this being legitimate because the singularity of the integrand at $(\hat{\theta}_0, 0)$ is excluded. We cannot, however, take this limit in the third term, which requires detailed treatment.

When $\theta - \hat{\theta}$ and ψ are both small, the equation (2.7) defining β shows that

$$\beta^2 = \left(\theta - \hat{\theta}\right)^2 + \sin^2\theta\psi^2 + \cdots, \qquad (3.4)$$

and we find that, on making use of the asymptotic expansion (2.11),

$$A\frac{\partial}{\partial\psi}\left(\psi\int_{\theta_0-\varepsilon}^{\theta_0+\varepsilon}\frac{f(\hat{\theta})P_n^{-1}(-\cos\beta)}{\sin\beta}\,\mathrm{d}\hat{\theta}\right) = c_0\mathrm{Re}\int_{x_0-\varepsilon}^{x_0+\varepsilon}\frac{f(x)\,\mathrm{d}x}{(z-x)^2} + O(\varepsilon\log\varepsilon), \qquad (3.5)$$

where Re denotes the real part, c_0 is defined in equation (2.12) and where $z = \theta + \mathrm{i}\psi$ and $x = \hat{\theta} + 0\mathrm{i}$ are local complex coordinates. We see that, as anticipated in §2, the singular part of the potential behaves as if the problem is plane. We now appeal to the extended Plemlj formula to enable us to take the limit and we have, for $\psi \geqslant 0$,

$$\lim_{z\to x_0}\int_{x_0-\varepsilon}^{x_0+\varepsilon}\frac{f(x)\,\mathrm{d}x}{(z-x)^2} = =\!\!\!\!\!\!\int_{x_0-\varepsilon}^{x_0+\varepsilon}\frac{f(x)\,\mathrm{d}x}{(x_0-x)^2} + \pi\mathrm{i}f'(x_0), \qquad (3.6)$$

so that

$$\frac{1}{\sin\theta}\frac{\partial\Phi}{\partial\psi} = A=\!\!\!\!\!\!\int_{-\gamma_0}^{\gamma_0}\frac{f(\hat{\theta})\,P_n^{-1}\left(-\cos(\hat{\theta}-\hat{\theta}_0)\right)}{\sin\left(\hat{\theta}-\hat{\theta}_0\right)}\,\mathrm{d}\hat{\theta} + O\left(\varepsilon\log\varepsilon\right), \qquad (3.7)$$

from which it follows, by letting $\varepsilon \to 0$, that the attached-flow problem is governed by the singular integral equation

$$=\!\!\!\!\!\!\int_{-\gamma_0}^{\gamma_0}\frac{f(\hat{\theta})\,P_n^{-1}\left(-\cos(\hat{\theta}-\hat{\theta}_0)\right)}{\sin(\hat{\theta}-\hat{\theta}_0)}\,\mathrm{d}\hat{\theta} = 0, \qquad -\gamma_0 \leqslant \hat{\theta}_0 \leqslant \gamma_0. \qquad (3.8)$$

The double stroke on the integral indicates the Hadamard principal part. We must treat the case $\hat{\theta}_0 = \gamma_0$ as the limit $\hat{\theta}_0 \to \gamma_0 - 0$ when evaluating the integral; similarly for $\hat{\theta}_0 = -\gamma_0$.

The solution of the integral equation must satisfy the requirement that $f(\hat{\theta})(\gamma_0^2 - \hat{\theta}^2)^{-1/2}$ is bounded as $\hat{\theta} \to \pm\hat{\gamma}_0$. We expect (3.8) coupled with this side condition to recover the BS solution. As a test of our formulation and because some of the implementation difficulties in the separated-flow case are anticipated in this simpler problem, we decided to solve (3.8) numerically.

3.2. *The Hadamard principal-part integrals*

The main difficulty is the evaluation of the Hadamard principal part integral. To evaluate the integrals, we constructed a cancellation function $C(\hat{\theta}, \hat{\theta}_0)$ by using (2.11) and the Taylor expansion of $f(\hat{\theta})$ about $\hat{\theta} = \hat{\theta}_0$; thus

$$C\left(\hat{\theta},\hat{\theta}_0\right) = \left(f(\hat{\theta}_0) + \delta f'(\hat{\theta}_0) + \tfrac{1}{2}\delta^2 f''(\hat{\theta}_0) + \cdots\right)\left(\frac{c_0}{\delta^2} + c_1 \log\frac{\delta^2}{4} + c_2' + \cdots\right), \quad (3.9)$$

where $\delta = \hat{\theta} - \hat{\theta}_0$, c_0 and c_1 are as defined in (2.12) and $c_2' = c_2 + c_0/6$; we retained terms of order one in δ in practice.

This treatment fails at $\hat{\theta}_0 = \pm\gamma_0$, and we replaced the cancellation function by

$$C_e\left(\hat{\theta},\gamma_0\right) = \left(g_0\delta^{1/2} + g_1\delta + g_2\delta^{3/2} + \cdots\right)\left(c_0/\delta^2 + \cdots\right). \quad (3.10)$$

Introducing the cancellation function into the singular integral equation (3.8) produces the integral equation

$$\int_{-\gamma_0}^{\gamma_0}\left(\frac{f(\hat{\theta})P_n^{-1}\left(-\cos(\theta-\hat{\theta}_0)\right)}{\sin(\hat{\theta}-\hat{\theta}_0)} - C\left(\hat{\theta},\hat{\theta}_0\right)\right)\mathrm{d}\theta + {=}\!\!\!\!\!\!\int_{-\gamma_0}^{\gamma_0} C(\hat{\theta},\hat{\theta}_0)d\hat{\theta} = 0,$$
$$-\gamma_0 \leqslant \hat{\theta}_0 \leqslant \gamma_0. \quad (3.11)$$

The integrand in the first integral in (3.11) is bounded (and has only a weak singularity of the form $\delta^2 \log\delta$). It can thus be evaluated by standard numerical methods. The second integral can be evaluated in closed form, using the rules for the evaluation of Hadamard integrals.

3.3. *Numerical solution*

We implemented two distinct schemes. Scheme A subdivided the range $0 \leqslant \hat{\theta} \leqslant \gamma_0$ into N equal intervals and took as unknowns $f = (f(0), f(\delta\hat{\theta}), \cdots, f(N\delta\hat{\theta}))$ where $\delta\hat{\theta} = \gamma_0/N$. Discretization of (3.11) using Simpson's rule leads to the non-standard eigenvalue problem

$$\boldsymbol{A}(n) f^T = 0, \quad (3.12)$$

where T denotes the transpose and $\boldsymbol{A}$ is an $(N+1) \times (N+1)$ matrix whose elements depend on n and γ_0. We used Gauss elimination to calculate $\det \boldsymbol{A}(n)$ and then used Newton's method to find n such that $\det(\boldsymbol{A}(n)) = 0$ to machine accuracy. More precisely, if n_0 is an initial estimate of n we iterate until

$$|\det(\boldsymbol{A}(n)) / \det(\boldsymbol{A}(n_0))| \leqslant 10^{-14}.$$

Because of the singular behavior of f as $\theta \to \gamma_0$, we obtained the derivative of f – and the coefficients in (3.10) – by fitting a polynomial of degree 3 in $y = (\gamma_0 - \hat{\theta})^{1/2}$ to the values of f near the tip.

Scheme B differed only in that a Glauert series, Glauert (1946, p. 138) was used,

$$f\left(\hat{\theta}\right) = \left(1 - \frac{\hat{\theta}^2}{\gamma_0^2}\right)^{1/2} \sum_{j=0}^{\infty} b_j \cos(2j\rho), \quad (3.13)$$

where

$$\cos\rho = -\hat{\theta}/\gamma_0,$$

thus building in the appropriate singularity.

We decided to compare with the results obtained for $\gamma_0 = \pi/4$ by BS. A recomputation of their formulation gave $n = 0.81465526$. Code A, using a 3-point series fit, with $N = 10$, 20, 40 and 80 and with extrapolation gave $n = 0.81466$. Code

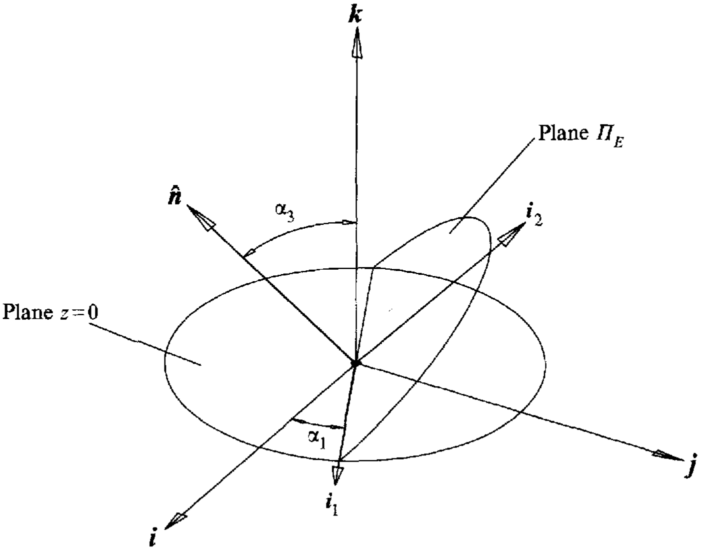

FIGURE 3. The geometry of the basic variables α_1 and α_3.

B, with a 10-coefficient expansion, gave $n = 0.814658$. Efforts to improve this result by taking more coefficients were not successful, possibly due to conditioning difficulties.

4. Description of the separated-flow problem

4.1. *The vortex sheets*

The separated inviscid flow is to be described by the introduction of two vortex sheets, one emanating from each edge of the delta wing. Each sheet is conical in shape and is expected to take the form of a conical spiral surface. The overall configuration is assumed symmetrical about the plane $y = 0$. We emphasize again that since $n < 1$, the flow is not conical in the sense that the velocity components are not constant along rays from the origin, but rather decay as R^{n-1}. We decided to represent the separated vortex sheets by plane elements E_s, each element having a linear distribution winglet strength. Our first task is to derive an efficient method of description of these elements.

Suppose that Π_E is the plane in which the element E_s lies. Let $\hat{n}$ be the unit normal to E_s and suppose that Π_E intersects the $(0, x, y)$-plane in a line whose unit vector is $\hat{i}_1$ (figure 3). We can then define an orthogonal triad $\hat{i}_1$, $\hat{n}$, $\hat{i}_2$, where $\hat{i}_2 = \hat{n} \wedge \hat{i}_1$. Then $\hat{i}_2$ lies in the plane Π_E also. Now $\hat{i}_1$ lies in the $(0, x, y)$-plane, so it must be of the form

$$\hat{i}_1 = (\cos\alpha_1, \sin\alpha_1, 0)\,; \tag{4.1}$$

α_1 is the first of our descriptive variables. We take as the second of our descriptive variables the angle α_3 between $\hat{n}$ and $\hat{k}$. We then find that

$$\hat{n} = (\sin\alpha_1 \sin\alpha_3, -\cos\alpha_1 \sin\alpha_3, \cos\alpha_3), \tag{4.2}$$

and

$$\hat{i}_2 = (-\cos\alpha_3 \sin\alpha_1, \cos\alpha_3 \cos\alpha_1, \sin\alpha_3). \tag{4.3}$$

We can now express the position x' of any point in the plane Π_E in terms of local polar coordinates (R', ρ'), where

$$x' = R'\left(\hat{\boldsymbol{i}}_1 \cos\rho' + \hat{\boldsymbol{i}}_2 \sin\rho'\right). \tag{4.4}$$

In particular, the element E_s can be defined by $\rho_1 \leqslant \rho' \leqslant \rho_2$. The polar angles ρ_1, ρ_2 comprise our third and fourth descriptive variables.

We can now express the velocity potential at a general point $\boldsymbol{x}$ on the unit sphere in terms of our chosen variables. We need only repeat the analysis of §2 to find

$$\Phi(\boldsymbol{x}) = \frac{n(n+1)}{4\pi}\cos\zeta \int_{\rho_1}^{\rho_2} \frac{P_n^{-1}(-\cos\beta)\, f(\rho')}{\sin\beta} \mathrm{d}\rho', \tag{4.5}$$

where

$$\begin{aligned}\cos\beta = {} & \cos\rho'(\cos\theta\cos\alpha_1 + \sin\theta\cos\psi\sin\alpha_1) + \sin\rho'(-\cos\theta\cos\alpha_3\sin\alpha_1 \\ & + \sin\theta\cos\psi\cos\alpha_3\cos\alpha_1 + \sin\theta\sin\psi\sin\alpha_3),\end{aligned} \tag{4.6}$$

and

$$\cos\zeta = \cos\theta\sin\alpha_1\sin\alpha_3 - \sin\theta\cos\psi\cos\alpha_1\sin\alpha_3 + \sin\theta\sin\psi\cos\alpha_3. \tag{4.7}$$

Here again, β is the geodesic distance between the field point $(\cos\theta, \sin\theta\cos\psi, \sin\theta\sin\psi)$ on the unit sphere and the point on the element E_s with local polar angle ρ. We note that if we set $\alpha_1 = 0$ and $\alpha_3 = 0$, these results reduce to those given in §2.

We plan to solve the problem by Newton iteration, so we must decide precisely how the positions of the elements E_s comprising the sheet are to be varied. Now in two dimensions (Pullin 1978) a successful strategy is to prescribe the angular positions of the vortex elements relative to the centre of the rolled-up portion of the vortex. We first choose the total angle τ, which we denote by τ_{M-1}, subtended by the set of elements $E_1, E_2, \cdots, E_{M-1}$ at P, the extremity of the final element E_M. Next, a subdivision of τ_{M-1} into $M-1$ subintervals $\mathrm{d}\tau_1, \mathrm{d}\tau_2, \cdots, \mathrm{d}\tau_{M-1}$, $\sum_1^{M-1} \mathrm{d}\tau_t = \tau_{M-1}$ is prescribed. Throughout the iteration the $\mathrm{d}\tau_t$ remain fixed, so each element continues to subtend its chosen sub-angle.

Adaptation of this procedure to spherical geometry is straightforward, but the formulae are cumbersome. In particular, the imposition of constant included spherical angle involves solving a transcendental equation.

4.2. *Pseudo-polar coordinates*

We bypassed this difficulty by introducing 'pseudo-polar' coordinates. Let (θ_s, ψ_s) be the spherical polar coordinates of the junction of the elements E_s and E_{s+1}. Define $(\hat{x}_s, \hat{y}_s)$ by

$$\hat{x}_s = \theta_s\cos\psi_s, \qquad \hat{y}_s = \theta_s\sin\psi_s, \tag{4.8}$$

and define $(\hat{x}_v, \hat{y}_v)$ by

$$\hat{x}_v = \theta_v\cos\psi_v, \qquad \hat{y}_v = \theta_v\sin\psi_v, \tag{4.9}$$

where (θ_v, ψ_v) are the spherical polar coordinates of P.

If we ignore curvature, we find

$$\hat{x}_s = \theta_v\cos\psi_v + r_s\cos\nu_s, \quad \hat{y}_s = \theta_v\sin\psi_v + r_s\sin\nu_s, \tag{4.10}$$

where r_s is the distance of the junction s from (θ_v, ψ_v), where

$$\nu_s = -\mu + \sum_{t=1}^{s} \mathrm{d}\tau_t, \qquad , s = 1, \cdots M-1, \tag{4.11}$$

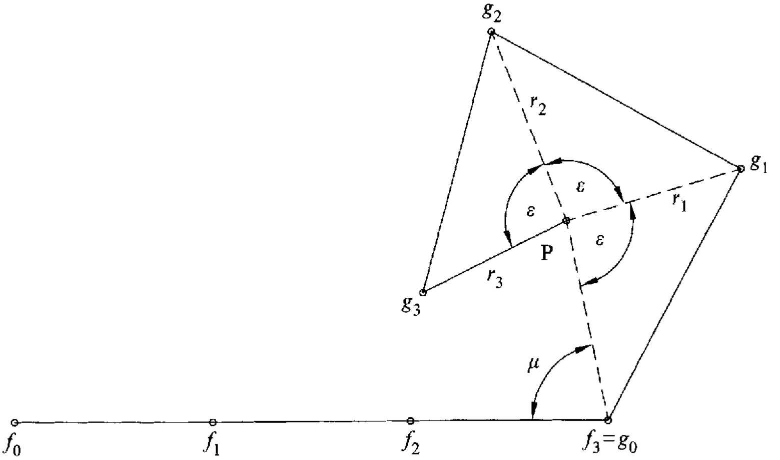

FIGURE 4. The case $N = 3$, $M = 4$ and $\mathrm{d}\tau_1 = \mathrm{d}\tau_2 = \mathrm{d}\tau_3 = \epsilon = \tau_3/3$. There are five geometric unknowns: r_1, r_2 and r_3, and the spherical polar coordinates θ_v, ψ_v of P, and six unknown winglet strengths: f_1, f_2, f_3 and g_1, g_2 and g_3.

and where μ is defined by

$$\cos\mu = (\gamma_0 - \theta_v \cos\psi_v)/\theta_v \sin\psi_v. \tag{4.12}$$

We now switch our point of view and regard (4.10)–(4.12) as *defining* (θ_s, ψ_s) in terms of r_s. It will not matter that in the variation the included spherical angles are not exactly preserved during variation of r_s and that r_s is not true geodesic distance.

We summarize our description of the geometry: let the subintervals $\mathrm{d}\tau_t, t = 1, \cdots M-1$ be specified. Then if (θ_v, ψ_v) are given and $r_s, s = 1, \cdots M-1$ are given then, first, μ can be calculated from (4.12), followed by $v_s, s = 1, \cdots M-1$ from (4.11). The values of $(\hat{x}_s, \hat{y}_s)$ can then be determined from (4.10) followed by calculation of $(\theta_s, \psi_s), s = 1, \cdots M-1$ from (4.8). Finally, we must express our parameters $\alpha_1^{(s)}$, $\alpha_3^{(s)}$, $\rho_1^{(s)}$ and $\rho_2^{(s)}$ defining element s in terms of the spherical polar coordinates $(\theta_{s-1}, \psi_{s-1})$ and (θ_s, ψ_s) of its edges. We give the details of the calculation in Appendix A, noting here only the point that care must be taken to ensure that the normal $\hat{\boldsymbol{n}}$ varies continuously as the sheet is traversed. Once the $\alpha_1^{(s)}$, $\alpha_3^{(s)}$, $\rho_1^{(s)}$ and $\rho_2^{(s)}$ are known, the contribution of each element E_s to the potential Φ and the velocity $\nabla\Phi$ at any point on the surface of the sphere can be calculated from (4.5).

We can now define the state of the discretized sheet. We can subdivide the semi-wing into N equal portions, each of angular extent γ_0/N. At the $N+1$ extremities of these portions we introduce winglets of strength $f_s (s = 0, 1, \cdots, N)$ with $f_0 = 1$ as a normalizing condition; since we are dealing with an eigenfunction, this step is essential. The elements E_1, E_2, $\cdots$, E_{M-1}, E_M have linear variations of winglet strengths over the ranges (f_N, g_1), (g_1, g_2), $\cdots$, (g_{M-2}, g_{M-1}), (g_{M-1}, g_{M-1}), where the terminal element has – for reasons discussed later – a constant winglet strength.

The state of the discretized flow is thus determined by the unknowns n, f_1, f_2, $\cdots$, f_N, g_1, g_2, $\cdots$, g_{M-1}, r_1, r_2, $\cdots$, r_{M-1}, θ_v, ψ_v; the case $N = 3$ and $M = 4$ is shown in figure 4. There are thus $N + 2M + 1$ unknowns, which must be determined from the boundary conditions. These boundary conditions are that the normal velocity vanishes at the $N+1$ points on the wing and the $2M$ conditions that the θ- and ψ-components of the vortex force vector on each element of the vortex sheet vanish (to some approximation). We discuss the boundary conditions in more detail in the next section.

5. The boundary conditions

5.1. *Boundary conditions on the wing*

Suppose that, as anticipated in §4, we represent the wing by $2N+1$ equally spaced winglets, the winglet strength distribution being symmetric, and the right-hand vortex sheet by M elements, on each of which there is a linear variation of winglet strengths, these strengths being continuous across the junctions of the elements (figure 4). The left-hand vortex sheet elements $\overline{E}_s$ are just mirror images of the right-hand vortex sheet elements E_s in the plane $y=0$.

Given this configuration, it is straightforward to calculate the velocity on the wing at the points $\hat{\theta} = s\gamma_0/N$, for $s = 0, 1, 2, \cdots, N-1$. The self-induced normal velocity is calculated by an appropriate modification of the method used to study the BS problem and (4.5) is used to calculate the contributions to the normal velocity on the wing from the elements E_s, $\overline{E}_s$ $(s = 1, 2, \cdots, M)$. However, the right-hand leading edge $\hat{\theta} = \gamma_0$ requires a more detailed discussion. To pursue this, we note that, according to the analysis of §3, the self-induced velocity $v_n(\hat{\theta})$ normal to the wing is given by the formula

$$2\pi v_n(\hat{\theta}) = -\frac{f(\gamma_0)}{\gamma_0-\hat{\theta}} + \frac{f(-\gamma_0)}{-\gamma_0-\hat{\theta}} + f'(\gamma_0)\log|\gamma_0-\hat{\theta}| - f'(\gamma_0)\log|\gamma_0+\hat{\theta}| + H(\hat{\theta}), \quad (5.1)$$

where $H(\hat{\theta})$ is bounded as $\hat{\theta} \to \pm\gamma_0$. We can see from this result that at the join of the wing to E_1 (or at the join of E_s and E_{s+1}) the singular terms will cancel if f and f' are continuous across the join.

By construction $f(\gamma_0) = g_0$, so the point-vortex terms cancel. However, we cannot force our solution to satisfy the condition $f'(\gamma_0) = g_0'$, so the log terms do *not* cancel. To deal with this, we compute the normal velocity at the join *as if* $f'(\gamma_0) = g_0'$ and then check the accuracy with which this consistency condition is satisfied in the converged solution.

We know from a local analysis (which to leading order is identical with the plane problem) that $f(\hat{\theta}) \approx f(\gamma_0)+a_1(\gamma_0-\hat{\theta})+a_2(\gamma_0-\hat{\theta})^{3/2}$, while the local form of the separating sheet is $\psi \approx h_2(\hat{\theta}-\gamma_0)^{1/2}$. Again, we cannot impose these properties on our solution, but we can examine the extent to which they are satisfied in the converged solution.

5.2. *Treatment of the free elements*

We now turn to the boundary conditions on the elements $E_1, E_2, \cdots, E_{M-1}$. We apply at the centre of each element the conditions

$$v_n = 0, \quad (5.2)$$

and

$$p_+ = p_-, \quad (5.3)$$

where '+' and '−' denote the two sides of the element and where v_n denotes normal velocity. Bernoulli's theorem enables (5.3) to be expressed in the form

$$n^2\Phi_+^2 + (v_t)_+^2 + (v_n)_+^2 = n^2\Phi_-^2 + (v_t)_-^2 + (v_n)_-^2, \quad (5.4)$$

where v_t is the tangential velocity. In view of (5.2), the pressure condition can be written as

$$n^2(\Phi_+ + \Phi_-)(\Phi_+ - \Phi_-) + ((v_t)_+ + (v_t)_-)((v_t)_+ - (v_t)_-) = 0. \quad (5.5)$$

or, denoting the mid-point of the element by 'm',

$$n^2 g_m \Phi_e + g_m'(v_t)_e = 0, \quad (5.6)$$

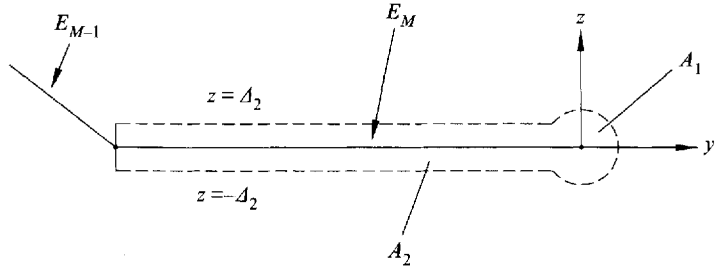

FIGURE 5. The intersection of the control volume with the surface of the unit sphere. The 'keyhole' domain is split, for convenience, into the 'barrel' A_1 and the 'slot' A_2.

where the suffix 'e' means that the self-induced contributions can be omitted in the calculation. This is legitimate since, for any distribution of winglet strength on a plane element, Φ is antisymmetric with respect to the plane. This is a considerable simplification in practice. Note however that the self-induced component of the normal velocity cannot be omitted in the implementation of (5.2).

5.3. *Inner portion of the sheet; the point vortex*

We must now discuss what is perhaps the major difficulty – the devising of an approximate representation of the tightly rolled-up inner portion of the vortex sheet. In two dimensions, the tightly wound portion can be represented by a point vortex, while in slender-body theory, a description of Brown & Michael (1959) type is possible. Our method is to devise a terminal element in the spirit of Brown & Michael's approach, although the details are more complicated.

We choose the terminal element E_M to have uniform winglet strength g_{M-1}. The spherical potential Φ then will, as was shown in §2, experience a jump g_{M-1} across the element which, to this extent, resembles the cut joining the point vortex to the wing in the Brown & Michael treatment. However, the vorticity in the element is not zero because of the presence of vorticity lying in the surface of the sphere.

We take as our boundary condition the vanishing of the vortex force on the element. To see why this is correct, we start by noting that Euler's equations give

$$\boldsymbol{\omega} \wedge \boldsymbol{u} = -\nabla H, \tag{5.7}$$

where $\boldsymbol{\omega}$ is the vorticity and H is the head. Thus for any control volume V bounded by a surface ∂V

$$\int_V \boldsymbol{\omega} \wedge \boldsymbol{u} \, \mathrm{d}V = -\int_{\partial V} H \hat{\boldsymbol{n}} \, \mathrm{d}S. \tag{5.8}$$

In Appendix B we show how the boundary conditions on E_M are derived from (5.8) and the geometry of figure 5. The final result is two equations, reproduced below as (5.9) and (5.10), which relate the induced velocity components at the central element V_E, W_E, and Φ_e to the other parameters of the problem:

$$-W_E + \frac{n g_{M-1}}{2\pi}\gamma = 0, \tag{5.9}$$

and

$$V_E - n^2 \gamma \Phi_e(0) = 0. \tag{5.10}$$

This approximation is consistent, since we expect the element E_M to shrink as the resolution is increased.

The problem is now completely formulated and we explain our numerical implementation in §6 and discuss our results in §7.

6. Numerical implementation

6.1. *Computation of* $P_n^{-m}(-\cos\theta)$

Both Scheme A and Scheme B require the rapid computation of the Legendre function $P_n^{-m}(-\cos\theta)$ in the range $0 < \theta < \pi$. Our method of achieving this was based on a table look-up. This exploits the representation of the Legendre function in terms of the hypergeometric function ${}_2F_1\left(-a, b, c, \cos^2(\frac{1}{2}\theta)\right)$ given in equation (2.10). This shows that the singular behaviour of the Legendre function as $\theta \to 0$ is due to the factor $\cot^m(\theta/2)$ so that interpolation on a table of hypergeometric function values should be adequate.

We divided the interval $[0, \pi]$ into $NTAB$ equal sub-intervals of size Δ. We computed table values at $\pi, \pi - \Delta, \pi - 2\Delta, \cdots$ using the power series expansion of the hypergeometric function, which was rapidly convergent, since $\theta/2$ was close to $\pi/2$. At $\pi - \theta = 0.2\pi$ we switched to integration of the hypergeometric differential equation – we could not start this integration at $\theta = \pi$ because of the regular singular point. This integration proceeded in the θ-increasing direction until the value 0.002π was reached. We then switched to the appropriate expansion, given by Abramovitz & Stegun (1964, p. 559), to cope with the regular singular point $\theta = 0$. We thus had two values of the hypergeometric function at the switch value of θ and we compared these as a running check, terminating the computation if the difference exceeded 10^{-9}.

Five-point Lagrange interpolation was used to provide the values of the Legendre function at a general value of θ. Some loss of accuracy can be expected near $\theta = 0$ because of the logarithmic terms in the expansion of the hypergeometric function. We used values of $NTAB$ in the range 5×10^3 to 10^4 to deal with this difficulty. The method was checked by comparison with values from MATHEMATICA and by verifying that the potential of a boundary element of uniform strength was a solution of (1.6).

6.2. *Scheme A*

Schemes A and Scheme B were independently adapted to the separated flow calculation, with the aim of providing mutual checks. We give brief details of these methods insofar as they differ from those already described for the attached flow. In Scheme A the interval $0 \leqslant \hat{\theta} \leqslant \gamma_0$ was divided into N intervals which were either of equal extent in $\hat{\theta}$ or which were clustered, using a cosine stretching, near the wing tip in order to increase locally resolution near the separation line. The influence integrals, of the type given by the left-hand side of (3.11) for field points on the wing, and by (4.5) for field points off the wing (at the mid-points of the sheet elements), were calculated by Simpson's rule. An exception was the calculation of the contribution of the wing to the normal velocity at the tip . Here a polynomial of degree 6 in $y = (\gamma_0 - \theta)^{1/2}$ of the form

$$f(\theta) = f(\gamma_0) + \sum_{j=1}^{6} a_j (\gamma_0 - \theta)^{(j+1)/2} \tag{6.1}$$

was fitted to f_i, $i = N-5, \cdots, N$. A special cancellation function was then constructed based on this form of $f(\hat{\theta})$ but with the log term omitted as described in §5 in relation to (5.1). The details are cumbersome but straightforward and are not given here. Integrals of the type (4.5) for Φ and for $\nabla\Phi$ give the velocity induced at the wing surface by the vortex sheet elements E_s and $\overline{E}_s$ (mirror image of E_s in the plane $y = 0$), $s = 1, \cdots M$. These integrals were calculated by subdividing each element E_s into N equal points and using Simpson's rule. Again $\theta = \gamma_0$ (wing tip) was exceptional, and here the contribution of each the first five elements $E_1, \cdots, E_5$ was computed with $4 \times N$-point Simpson's rule to provide extra accuracy for this sensitive calculation. This gives $(N + 1)$ residuals.

The boundary conditions (5.2) and (5.6) were applied at the element midpoints $s = 1, \cdots M - 1$ as follows. First the midpoint of the ith element, E_i, and the two unit vectors at this midpoint normal to the element, and tangential to both the element and the sphere, were determined. Next Φ, $\nabla\Phi$ at the ith midpoint were calculated from contributions of the wing and of the sheet element sets E_s, $\overline{E}_s$, $s = 1, M$. The normal self-induced velocity was calculated using the cancellation function of the type (3.9) adapted to the linear f-distribution on the element. Resolving in the normal and tangential directions and taking care to omit the self-induced tangential velocity and potential of E_i as described in §5 then gives $(\Phi_e, v_n, (v_t)_e)$ at the midpoint. For the right-hand element set, all integrals were calculated by N-point Simpson's rule, while for the left-hand set $N/4$-point Simpson's rule was used after having checked that this entailed no loss of accuracy. Equation (5.2) then provided $M - 1$ residuals, and (5.6) in the approximate form

$$\tfrac{1}{2} n^2 (g_{i-1} + g_i)\, \Phi_e + (g_i - g_{i-1})\,(v_t)_e = 0 \tag{6.2}$$

provided a further $M - 1$ residuals. Finally (5.9) and (5.10) were applied, calculating all relevant integrals as for the application of (5.2) andd (5.6), giving a further 2 residuals, making a total of $N + 2M + 1$, which when forced to zero, will determine the $N + 2M + 1$ unknowns $n, f_1, f_2, \cdots, f_N, g_1, g_2, \cdots, g_{M-1}, r_1, r_2, \cdots, r_{M-1}, \theta_v, \psi_v$.

In Scheme A the residuals were forced towards zero using Newton iteration. Convergence was accepted when

$$\max_{(0<k\leqslant N+2M+1)} |\mathscr{R}_k| \leqslant \epsilon, \tag{6.3}$$

where $\mathscr{R}_k$ is the kth residual and ϵ a specified tolerance. Generally $\epsilon = 10^{-10}$, but this could not always be achieved (see §7). The Jacobian was constructed along with the residuals using a combination of analytic and centred finite-difference methods. We shall characterize the Scheme A solutions by the notation $[N, M - 1, m_T]$, where $m_T \approx \tau_{M-1}/(2\pi)$ is the number of complete turns of the sheet represented by τ_{M-1}, the total pseudo-angular extent of the rolled-up portion of the vortex sheet. In some cases to be discussed the angular extents of the sheet elements were not uniform over its whole extent but were somewhat clustered near the tip. The average number of sheet elements per turn is approximately $(M - 1)/m_T$. The strategy used to obtain solutions was to start with the attached flow solution for $\gamma_0 = \pi/4$, and then guess the position of the central vortex for $[N, M - 1, m_T] = [32, 0, 0]$, corresponding to a Brown–Michael (1959)-type solution with only a single plane winglet connecting the wing edge to the central vortex. With some experimentation this was successful, leading to a converged solution. Then a solution with $[N, M - 1, m_T] = [32, 5, 0.25]$ was found by guessing the local shape and strength of a small sheet emanating from the tip. Once this solution was found, initial approximations for solutions with increasing M were generated by extrapolation of the sheet shape and strength from those with smaller M. When several turns of the sheet were generated, the asymptotic inner form of the spiral (see §7) was fitted to the solution and the sheet extended further.

6.3. *Scheme B*

The objectives of Scheme B were two-fold. The first and most important objective was to provide a check on Scheme A. Apart from the routines to calculate the Legendre functions, which could be readily checked as described, the two codes were completely independent. The second objective was to test the robustness of our formulation against changes of detail at the point of greatest vulnerability, which we believe to be the wing tip. With this view, we replaced the boundary condition of zero normal velocity by the requirement that $\mathrm{d}f/\mathrm{d}\sigma$ be continuous at the tip, where σ is arclength along the sheet. Also, the structure of Scheme B enabled us to force the correct singularity in the behaviour of f as $\theta \rightarrow \gamma_0$.

The motivation for Scheme B starts from the observation that a plausible expansion for the winglet strength $f(\theta)$ is

$$f(\theta) = \hat{a}_0 + \hat{a}_1 y + \hat{a}_2 y^2 + \hat{a}_3 y^3 + \hat{a}_4 y^4 + \cdots, \tag{6.4}$$

where $y = \left(1 - (\theta/\gamma_0)^2\right)^{1/2}$. If $\hat{a}_1 = 0$, then $f(\theta)$ has the correct behaviour at the wing tips $\theta = \pm\gamma_0$. However this form would be ill-conditioned and we changed to the Glauert variable given by

$$\cos\rho = -\frac{\theta}{\gamma_0}, \tag{6.5}$$

and expressed the expansion in the form

$$f = \hat{b}_0 + \hat{b}_1\theta^2 + \sin^3\rho\left(\hat{c}_0 + \hat{c}_1\sin\rho + \hat{c}_2\sin^2\rho + \cdots\right). \tag{6.6}$$

Formally, we can re-expand the series in the above equation as a half-range cosine series in which only even terms arise by symmetry. Thus we arrive at the form used in Scheme B. This is

$$f = \hat{b}_0 + \hat{b}_1\theta^2 + \sin^3\rho\left(\hat{d}_0 + \hat{d}_1\cos 2\rho + \hat{d}_2\cos 4\rho + \cdots\right). \tag{6.7}$$

Unfortunately the series cannot be expected to converge rapidly, because the half-range expansion of $\sin\rho$ has an j^{th} Fourier coefficient of order j^{-2}. Since the series must be twice differentiated to obtain the f-derivatives needed in the construction of the cancellation function it is surprising that the ansatz performed as well as it did.

An advantage of this indirect representation is that the number of integration points on the semi-wing $NMESH+1$ is not restricted to the number of points $N+1$ at which boundary conditions were satisfied. However the number of coefficients in the truncated form of the expansion must be $N+2$, to cope with the N zero normal velocity conditions at internal points of the semi-wing, the condition of continuity of $\mathrm{d}f/\mathrm{d}s$ and the normalization condition on f.

In calculating the effect of the left-hand sheet winglets on the wing and the right-hand sheet, Simpson's-rule integration with 8 points was used. Simpson's integration with $2N+1$ points was used for calculating the effect of each right-hand winglet on its neighbours and on the wing. However an analytical approximation, whose error was $O(\rho^4\log(\rho))$ for a winglet of angular extent ρ, was used to calculate the self-induced velocity of each winglet. A numerical one-sided Jacobian was used to simplify the coding at the expense of greatly increased computing time. In view however of the schemes limited role, this inefficiency was acceptable.

At first the boundary conditions on the wing were satisfied at equally spaced points on the wing, but conditioning was poor. Following a suggestion of Dr A. Iserles, points

N	$NMESH$	n	θ_v	ψ_v
8	128	0.58541	0.72624	0.37454
16	256	0.58518	0.72661	0,37450
32	512	0.58506	0.72680	0.37448
64	1024	0.58707	0.72368	0.37480
64	2048	0.58503	0.72684	0.37447
Scheme A	Extrapolated	0.58491	0.72713	0.37437

TABLE 1. Comparison of Scheme A and Scheme B. All the runs had $M = 21$. First five rows are Scheme B results. The Scheme A results are Richardson extrapolated to infinite N assuming that the error is proportional to N^{-1}. The reason why extra integration points are needed in the case $N = 64$ is not known.

equally spaced in the Glauert variable r were used and this cured the conditioning difficulty. It transpired that a very large number of integration points were needed to cope with the rapid oscillations of the cosine functions near the wing tips, the spacing of which, in θ, was $O(N^{-2})$. Better results were obtained with integration points spaced equally in ρ, but the table size had to be large enough to ensure that interpolation in the last few intervals was avoided, for the reason given previously. A comparison with a special run of Scheme A in which $M - 1$ was fixed at 21 and N varied is shown in table 1. The agreement is satisfactory.

7. Results and discussion

7.1. *The case* $\gamma_0 = \pi/4$

We seek numerical approximations to an exact solution with both f and the shape of the sheet continuous. We recognize however, that an exact solution will contain arbitrarily small length scales within the inner rolled-up portion $\tau > \tau_{M-1}$ (represented here by the plane terminal element E_M) which are unresolved with any finite choice of m_T. It is our aim, not always achieved here, to construct solutions with numerical values of $[N, M-1, m_T = 1]$ sufficiently large so as to achieve at least three-figure-accurate numerics. In order to discuss the basic properties of our numerical solutions we begin with Scheme A solutions for $\gamma_0 = \pi/4$. We discuss two classes of solution, the first of the form $[N, M-1, m_T = 1]$ for Scheme A with N and M increasing uniformly, in order to demonstrate convergence with a fixed extent of the sheet. These are summarized in table 2 ($\gamma_0 = \pi/4$), which shows the variation of the solution parameters (n, θ_v, ψ_v) with N, M. Also shown are the values obtained by Richardson extrapolation from the $[64, 20, m_T = 1]$ and $[128, 40, m_T = 1]$ solutions, assuming convergence as $(1/N)^2$. There is satisfactory agreement between the calculated and extrapolated values for the $[256, 80, m_T = 1]$ solution. The value tabulated as $[\infty, \infty, m_T = 1]$ may be assumed third-order accurate in $1/N$. It may be seen that convergence to three-figure accuracy is achieved with the $[128, 40, m_T = 1]$ solution. We conclude that, *with* τ_{M-1} *fixed*, we can obtain three-figure accuracy with about 35 points per turn of the sheet. In figure 6 we show the vortex sheet shapes in the (θ, ψ)-plane plane for these solutions. The shapes for the $[128, 40, m_T = 1]$ and $[256, 80, m_T = 1]$ solutions are indistinguishable on the plotting scale shown.

Next we keep $N = 128$ fixed and the number of sheet elements per turn $(M-1)/m_T$ fixed at about 35, and increase m_T. Table 3 shows the principal parameters for this sequence of solutions. Convergence is not monotonic as m_T is increased, at least

N	$M-1$	m_T	n	θ_v	ψ_v
64	20	1	0.585203	0.726605	0.374477
128	40	1	0.586281	0.725343	0.373749
256	80	1	0.586591	0.724987	0.373549
256	80	1	0.586551	0.725028	0.373567
∞	∞	1	0.586640	0.724922	0.373506

TABLE 2. Principal solution parameters for Scheme A solutions $[N, M-1, m_T = 1]$ with $\gamma_0 = \pi/4$. The fourth row gives the values obtained by Richardson extrapolation from the $[64, 20, m_T = 1]$ and $[128, 40, m_T = 1]$ solutions assuming convergence as $(1/N)^2$. The fifth row shows extrapolation to $N = \infty$.

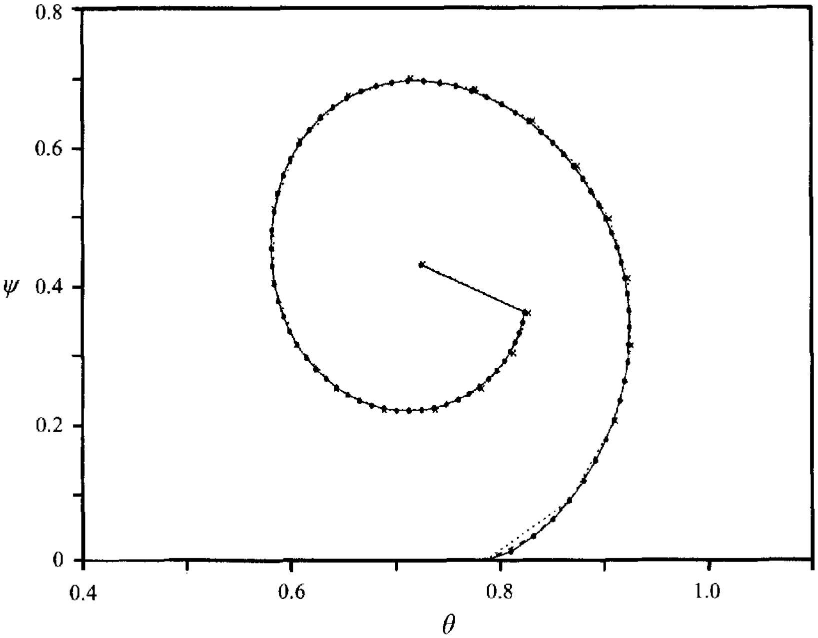

FIGURE 6. Vortex sheet shapes in the (θ, ψ)-plane, $\gamma_0 = \pi/4$. All three solutions have $\tau_{M-1} = 7.3684210$. ×, $[N, M-1, m_T] = [64, 20, 1]$; ▲, $[N, M-1, m_T] = [128, 40, 1]$; •, $[N, M-1, m_T] = [256, 80, 1]$.

N	$M-1$	m_T	n	θ_v	ψ_v
128	41	1	0.585622	0.723412	0.370934
128	75	2	0.581320	0.724428	0.369761
128	109	3	0.579629	0.724317	0.369006
128	143	4	0.578946	0.724417	0.368779
128	177	5	0.578583	0.724472	0.368644
128	211	6	0.578369	0.724507	0.368555

TABLE 3. Principal solution parameters for Scheme A solutions $[N, M-1, m_T = 1]$ with $N = 128$ fixed and m_T increasing. $\gamma_0 = \pi/4$. The number of elements per turn of the sheet $(M-1)/m_T$ is held nearly constant at about 35.

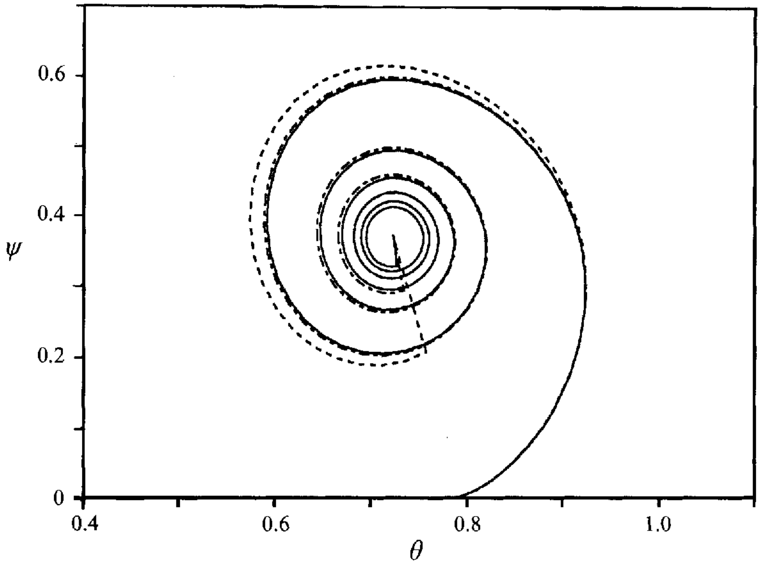

FIGURE 7. Vortex sheet shapes in the (θ,ψ)-plane, $\gamma_0=\pi/4$. ———, $[N,M-1,m_T]=[128,211,6]$; — - — - —, $[N,M-1,m_T]=[128,109,3]$; - - - - -, $[N,M-1,m_T]=[128,41,1]$.

for θ_v. The $[128,109,m_T=3]$ solution gives three-figure-accurate approximations to our most refined solution, $[128,211,m_T=6]$, except for n, where the discrepancy is of order 0.2%. In figure 7 we compare the shapes for solutions with $m_T=1,3,6$. The shape of the outer turn for the $m_T=1$ solution is rather different from that for $m_T=6$ solutions; note that these differences are much larger than the corresponding discrepancies between the corresponding (θ_v,ψ_v) positions in table 3. It may also be seen that there are significant differences when comparing (θ_v,ψ_v) values of the $[128,41,m_T=1]$ solution of table 3 with the $[128,40,m_T=1]$ solution of table 2. This is because the the extent of the sheet, given by τ_{M-1}, is different for the two solutions as may be seen by comparing the shapes in figures 6 and 8. This difference in extent is due to the fact that the elements of the $[128,41,m_T=1]$ solution are of nonuniform angular extent, having been clustered near the wing tip in order to improve accuracy for production runs. This can be seen in figure 8 which shows details of the vortex sheet for three solutions near the wing tip. There is good agreement in this region. In figure 9 we display the variation of winglet strength $f(\sigma)$ along the right half-wing and along the vortex sheet, where σ is the arclength along the intersection of the conical wing–sheet surface with the unit sphere, measured from the wing tip. Values $\sigma\leqslant 0$ correspond to the wing. The tangential velocity difference across the composite wing–separated flow vortex sheet $\mathrm{d}f/\mathrm{d}\sigma$ (the wing is of course also a conical vortex sheet that can support a pressure difference) can be seen to change sign just inboard of separation. It will be later seen that the occurrence of $\mathrm{d}f/\mathrm{d}\sigma=0$ very near the tip is characteristic of all numerical solutions discussed here. A detail of the maximum in $f(\sigma)$ for three solutions with $\gamma_0=\pi/4$ is shown in figure 10 from which it may be seen that the numerics produce a smooth variation of $\mathrm{d}f/\mathrm{d}\sigma=0$ at the tip as required (see discussion following (5.1)), at least on the plotting scale. This will be discussed further later. The $[128,109,m_T=3]$ and the $[128,211,m_T=6]$ solutions show agreement to four figures in f-values near the tip.

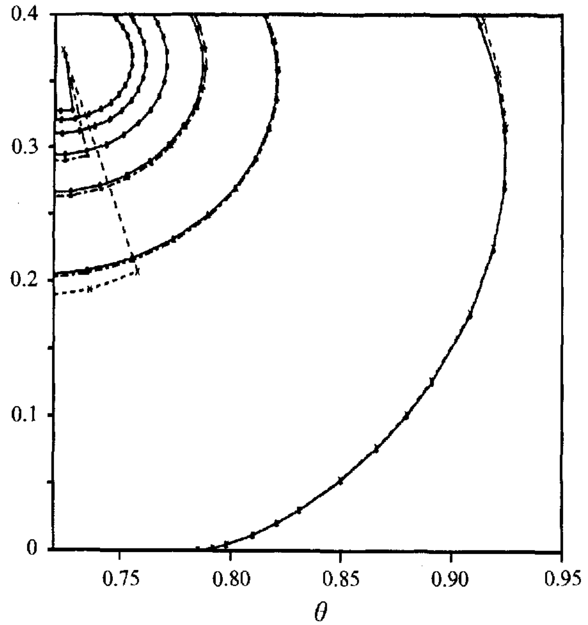

FIGURE 8. Near-tip detail in the (θ, ψ)-plane, $\gamma_0 = \pi/4$. ———, •, $[N, M-1, m_T] = [128, 211, 6]$; — - — - —, ▲, $[N, M-1, m_T] = [128, 109, 3]$; - - - - -, ×, $[N, M-1, m_T] = [128, 41, 1]$.

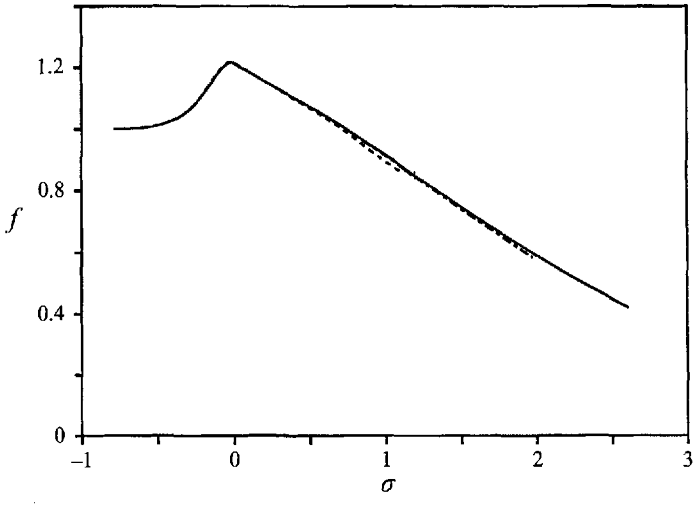

FIGURE 9. Winglet strength f versus arclength σ along the line of intersection of the right half-wing and vortex sheet with the unit sphere, $\gamma_0 = \pi/4$. σ is measured from the tip and is negative on the wing and positive on the separated sheet. ———, $[N, M-1, m_T] = [128, 211, 6]$; — - — - —, $[N, M-1, m_T] = [128, 109, 3]$; - - - - -, $[N, M-1, m_T] = [128, 41, 1]$.

7.2. $0 < \gamma_0 < \pi/2$

The results of the previous subsection indicate that at least three-figure accuracy in all computed quantities can be obtained with $[128, 109, m_T = 3]$ so these parameters were used, where possible, for a range of values of γ_0. Continuation in γ_0 using two-, three- and four-point extrapolation was achieved without difficulty for $\gamma_0 < 45°$ down to a minimum of $\gamma_0 = 1.3°$ below which, even with four-point extrapolation used to

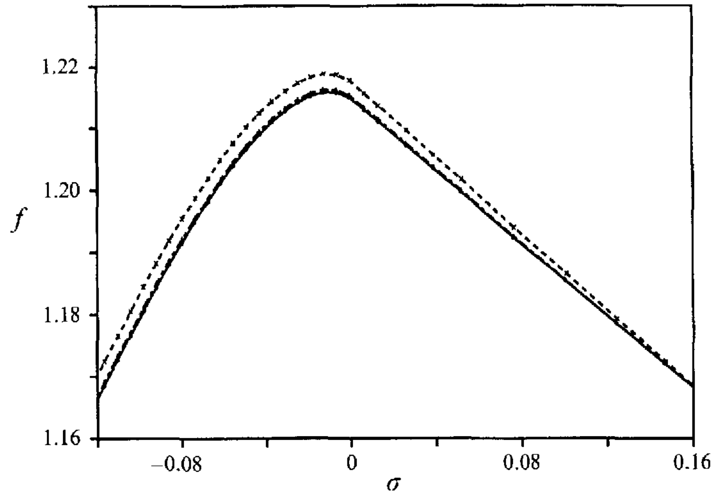

FIGURE 10. Detail of figure 9 near the wing tip, $\gamma_0 = \pi/4$. ————, •, $[N, M-1, m_T]$ =[128,211,6]; — - — - —, △, $[N, M-1, m_T] = [128, 109, 3]$; - - - - -, ×, $[N, M-1, m_T] = [128, 41, 1]$.

N	$M-1$	m_T	γ_0	n	θ_v	ψ_v
128	109	3	0.049087(2.8°)	0.99628	0.070612	0.90765
128	109	3	0.261799(15°)	0.92728	0.25109	0.61406
128	109	3	0.523599(30°)	0.75441	0.48041	0.43040
128	211	6	0.785398(45°)	0.57837	0.72451	0.36856
128	109	6	1.04720(60°)	0.44010	0.96811	0.36308
128	43	1	1.30900(75°)	0.33643	1.2006	0.39342
128	43	1	1.56207(89.5°)	0.23975	1.4003	0.45947

TABLE 4. Principal solution parameters for Scheme A solutions $[N, M-1, m_T = 1]$, various γ_0.

estimate the starting approximation for the next γ_0, very small values of the increment in γ_0 of order $\delta\gamma_0 = O(0.01°)$ were required for further calculation. Figure 11 shows perspective views of the conical wing–sheet surface for selected values of γ_0. The corresponding parameters n, θ_v and ψ_v are listed in table 4.

We found no difficulty in continuation for $\gamma_0 > 45°$ to about $\gamma_0 = 62°$ for Scheme A. For larger γ_0 however, continuation failed even with four-point extrapolation and very small $\delta\gamma_0$. We found no indication of a turning point in γ_0 which might indicate non-uniqueness, and no onset of large gradients in the solution parameters with increasing γ_0 which might signal a change in the global character of solutions in this range of γ_0. In order to overcome this problem, a new $[64, 43, m_T = 1]$ solution was constructed at $\gamma_0 = 75°$ using the method of extrapolation from an $M = 1$ solution described in §6 in relation to $\gamma_0 = 45°$. It was found that this could be continued to $\gamma_0 \approx 89.9°$, but failed for $\gamma_0 = 90°$ owing to an apparently nearly singular Jacobian. We remark that the apex singularity vanishes at $\gamma_0 = 90°$. It was observed that the convergence of the Newton method degraded significantly as $\gamma_0 \rightarrow 90°$ and this was associated with non-convergence to $\epsilon = 10^{-10}$ (see (6.3)). For example the present 'solution' for $\gamma_0 \approx 89.5°$ tabulated in table 4 and shown in perspective view in figure 11 converged only to $\epsilon \approx 10^{-8}$. Several attempts to find solutions for $\gamma_0 > 90°$ failed.

Figure 12 shows the winglet strength $f(\sigma)$ for the solutions tabulated in table 4. In

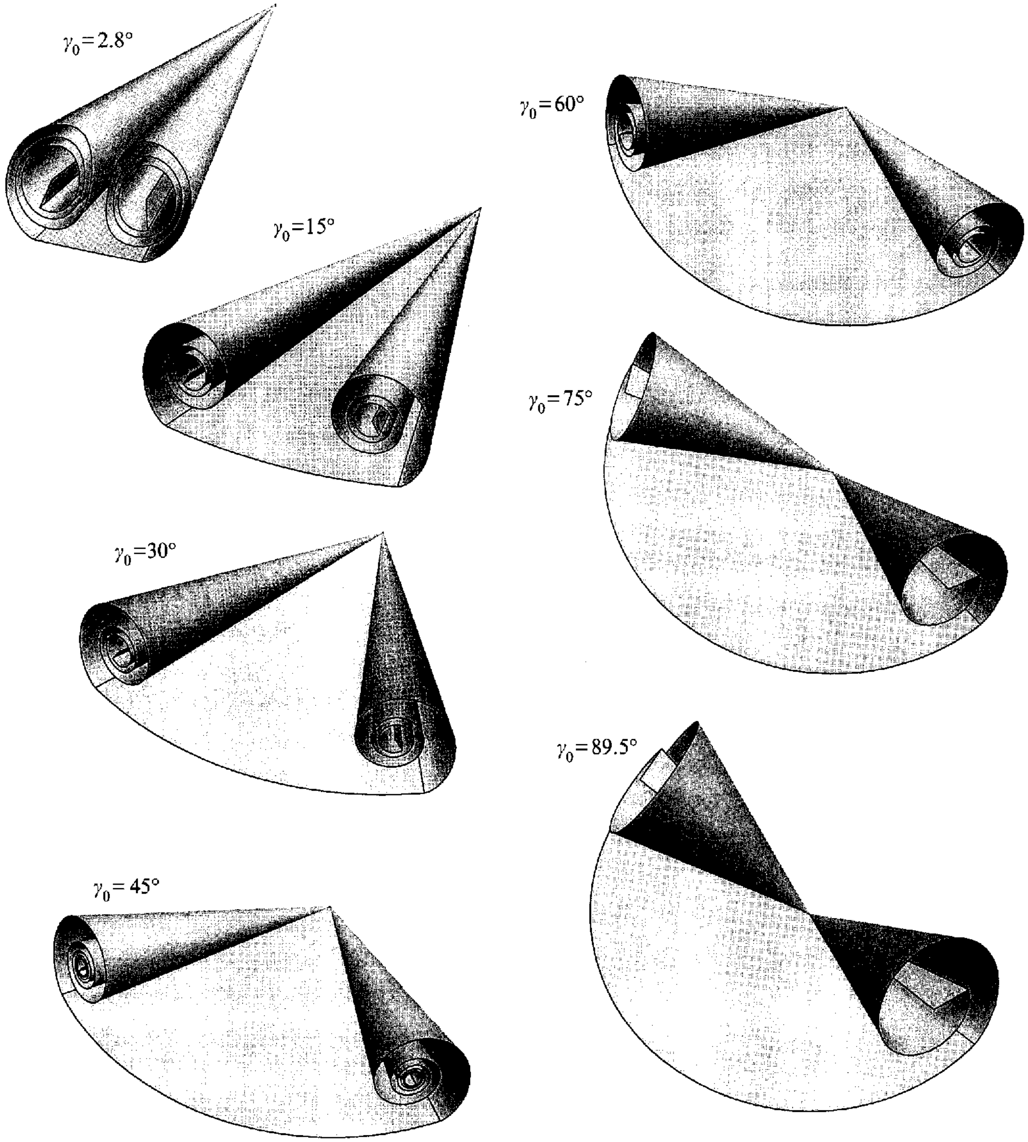

FIGURE 11. Perspective views of wing and conical vortex sheets for solutions of table 4. Values of γ_0 as indicated. View angle and scale differ slightly for each case.

all cases $\mathrm{d}f/\mathrm{d}\sigma$ may be seen to vanish just inboard of the wing tip. Some insight into the behaviour of solutions in the vicinity of the tip may be obtained by appealing to the properties of a local solution in this region. This is outlined in Appendix C, where it is shown that the local form of the potential $\Phi^{\pm}$ above and below the wing surface is related to the leading-order shape of the separated vortex sheet. These *local identities* are given by equations (C12) whilst the corresponding local sheet shape is given by (C14). The quantities $C^{\pm}$ were estimated by fitting polynomials of the form

$$\Phi^{\pm}(\theta)=\Phi^{\pm}(\gamma_0)+\sum_{j=0}^{6} b_j\,(\gamma_0-\theta)^{(j+1)/2}, \tag{7.1}$$

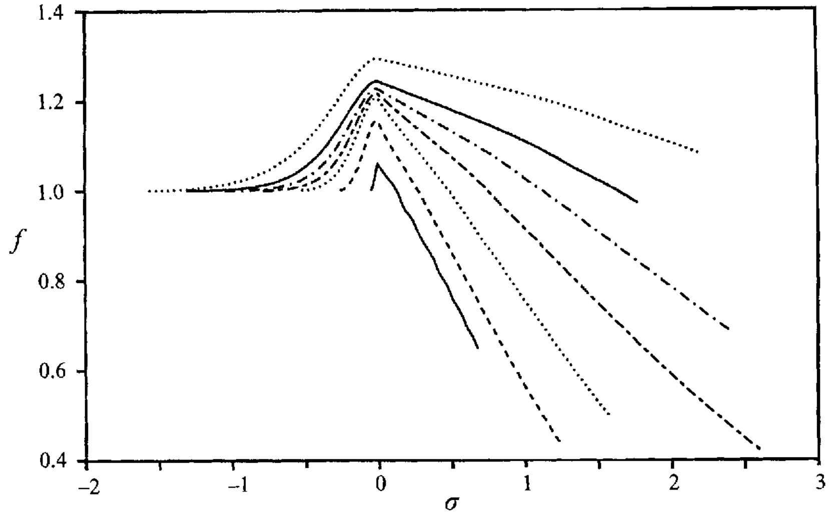

FIGURE 12. Winglet strength f versus arclength σ along the line of intersection of the right half-wing and vortex sheet with the unit sphere for solutions of table 4. Values of γ_0 increase with f at $\sigma = 0$. $\gamma_0 = 2.8°, 15°, 30°, 45°, 60°, 75°, 89.5°$.

together with a corresponding polynomial for $f(\theta)$, to the calculated values near the tip from the numerical solutions. In comparison with (6.1), note the inclusion of a term in $(\gamma_0 - \theta)^{1/2}$. Values of $C^{\pm}$ obtained by estimating $U_{\pm}$ and $\alpha_{\pm}$ (see (C7)–(C8)) from the calculated coefficients and use of (C12), are tabulated in table 5. Also shown are corresponding values of $C(sheet)$ obtained by a least-square fit of the form (C14) to the calculated values of θ, ψ on the first few points of the separated sheet near the tip. The agreement in table 5 is only fair. In order to test for power-law behaviour of the sheet shape near the tip, we plot, in figure 13, the shape in the form ψ versus $\theta - \gamma_0$ on log-log axes. In all cases the 3/2 power-law form of (C14) is evident near the tip. Table 6 compares values of $(\mathrm{d}f/\mathrm{d}\sigma)^-_{\gamma_0}$ calculated from the $\gamma_0 - \theta$ term in the polynomial for f and $(\mathrm{d}f/\mathrm{d}\sigma)^+_{\gamma_0} = (g_1 - g_0)/(\sigma_1 - \sigma_0)$ obtained from the first sheet element. This discrepancy is one measure of the lack of consistency of our treatment of the separation region. Table 6 also gives values of $(\gamma_0 - \theta)$ at which f shows a maximum near the wing tip and the value of the coefficient of $(\gamma_0 - \theta)^{1/2}$ in the polynomial fit to f. In an exact solution this is expected to be zero. A finite, albeit numerically small, value indicates a residual singularity in the near-tip numerical solution, characteristic of attached flow. We suspect but are unable to prove that the presence of this small coefficient in our numerical results, not explicitly recognized in the formulation, may account for the somewhat poor performance of Newton's method in some cases.

Appendix D gives an analysis of the asymptotic behaviour of the inner part of the rolled-up conical vortex sheet. The principal result (D10) shows that, surprisingly, the sheet shape, in local spherical coordinates with polar axis aligned with the axis of roll-up, is of power-law form with exponent (−1) independent of n. In order to test this we fitted a least-squares best-fit curve of the form

$$r_s = A(\nu - \nu_0)^{-\mu_1}\left(1 + \varepsilon_1 \cos\big(2(\nu - \nu_1)\big) + \varepsilon_2 \cos\big(2(\nu - \nu_2)\big)\right) \tag{7.2}$$

to the inner four turns (so as to reduce end effects) of our six-turn solution for $\gamma_0 = 45°$. In (7.2) r_s is the radius defined by (4.10), ν is the pseudo-polar angle and

γ_0	C^+	C^-	$C(sheet)$
0.049087(2.8°)	4.10	5.08	3.86
0.261799(15°)	3.51	3.34	3.22
0.523599(30°)	2.75	2.58	2.59
0.785398(45°)	2.10	2.13	2.23
1.04720(60°)	1.64	1.80	1.80
1.30900(75°)	1.76	2.16	1.66
1.56207(89.5°)	1.29	1.64	1.45

TABLE 5. Identities. $C^\pm$ estimated by polynomial fit to $\Phi\pm$ near wing tip. $C(sheet)$ estimated from fit of form $\psi = C/(\sin\gamma_0)^{-1}(\theta-\gamma_0)^{3/2}$ to first two points on free vortex sheet.

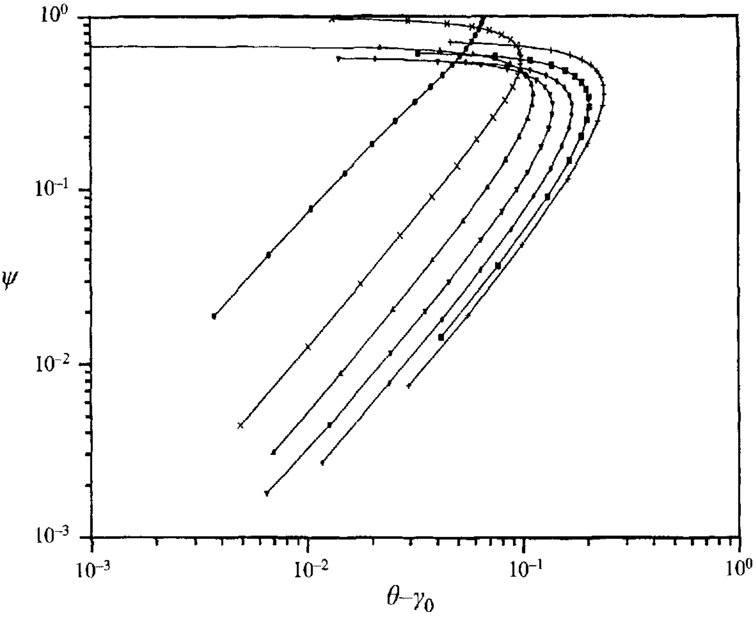

FIGURE 13. Shape of separated sheet near tip in the form of ψ versus $\theta-\gamma_0$. •, $\gamma_0 = 2.8°$; ×, $\gamma_0 = 15°$; ▲, $\gamma_0 = 30°$; ▼, $\gamma_0 = 45°$; ◆, $\gamma_0 = 60°$; ■, $\gamma_0 = 75°$; +, $\gamma_0 = 89.5°$.

γ_0	$\left(\frac{\mathrm{d}f}{\mathrm{d}\sigma}\right)^-_{\gamma_0}$	$\left(\frac{\mathrm{d}f}{\mathrm{d}\sigma}\right)^+_{\gamma_0}$	$(\gamma_0-\theta)_{max}$	b_0
0.049087(2.8°)	−0.713	−0.657	0.523×10^{-3}	-0.241×10^{-3}
0.261799(15°)	−0.737	−0.705	0.609×10^{-2}	-0.335×10^{-3}
0.523599(30°)	−0.513	−0.488	0.837×10^{-2}	-0.288×10^{-3}
0.785398(45°)	−0.326	−0.308	0.766×10^{-2}	-0.148×10^{-3}
1.04720(60°)	−0.205	−0.192	0.652×10^{-2}	-0.744×10^{-4}
1.30900(75°)	−0.130	−0.125	0.425×10^{-2}	-0.724×10^{-4}
1.56207(89.5°)	−0.083	−0.076	0.306×10^{-2}	-0.738×10^{-4}

TABLE 6. Selected properties of solutions at the wing tip. $(\gamma_0-\theta)_{max}$ is the angle at which $\mathrm{d}f/\mathrm{d}\sigma = 0$ on the wing. b_0 is the calculated coefficient in a polynomial fit of degree 7 in $y = (\gamma_0-\theta)^{1/2}$ near the wing tip

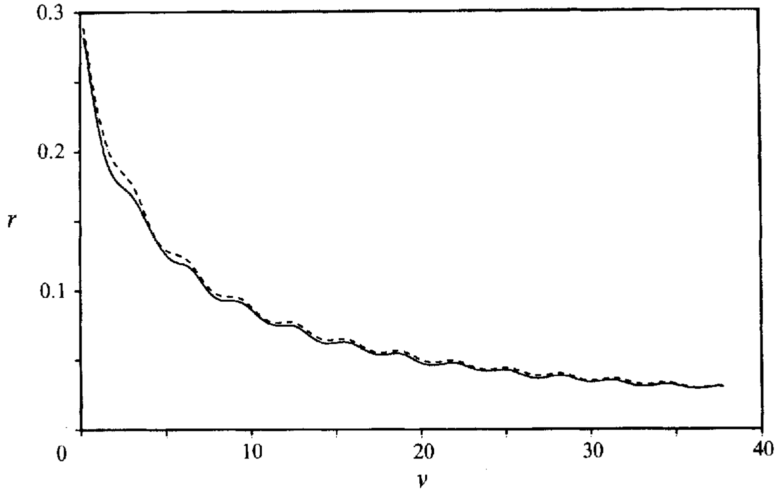

FIGURE 14. Radius r of vortex sheet measured as the angle subtended at the sphere centre by a point on the sheet and the isolated vortex (axis of rollup), versus pseudo-polar angle ν. $\gamma_0 = 45°$. ———, computation; – – – – –, five-parameter least-squares fit.

A, μ_1, ν_0, ν_1, ν_2, ε_1 and ε_2 are parameters to be determined from the least-squares fit. Note that (r_s, ν) are not identical with $(r, \bar{\varphi})$ of (C10) but will be good approximations to these quantities for small r and large $\bar{\varphi}$. From the least-squares fit we obtain $\mu_1 = 0.982$, in satisfactory agreement with the exponent in (C10), and $A = 1.093$, $\nu_0 = -3.553$, $\nu_1 = -0.216$, $\nu_2 = 0.142$, $\varepsilon_1 = 0.038$, $\varepsilon_2 = 0.001$. A five-parameter fit $(\varepsilon_2 = 0)$ gave $\mu_1 = 0.977$. Figure 14 compares the variation of r_s with ν obtained from the numerical solution to (7.2) with the parameters given above.

7.3. *Topology of the (v_θ, v_φ) field*

One method of visualizing the flow produced by the eigensolutions is to plot the streamlines of the (v_θ, v_φ) velocity field on the surface of the unit sphere. This is done in figures 15 and 16 for $\gamma_0 = 2.8°$, 45° and 89.5° where streamlines on the hemisphere $x > 0$ are shown viewed along the positive x-axis. Also shown in figure 16 are the contours of Φ on this hemisphere. Recall that v_R is proportional to $n\Phi$. The topology of the streamline pattern can be characterized by the number, type and position of the critical points of the (v_θ, v_φ) field on the sphere and this in turn then gives information on how the flow approaches and leaves the wing-sheet surface from infinity. The detailed topology depends on γ_0. In all cases there are two sink-like spiral nodes at the vortex centres where the flow escapes to $R = \infty$. In figure 15, for $\gamma_0 = 2.8°$ there are saddle points on either side of the wing centre line and a saddle point on the symmetry axis above the wing–sheet system. Following back the streamlines from this saddle demarcates that part of the local flow which is entrained into the vortex from that which flows past the wing.

When $\gamma_0 < 13°$ there were found to be three additional critical points lying on the intersection of the sphere with the (x, z)-plane. We denote these by C_1, C_2 and C_3 respectively: C_1 is source-like, C_2 is sink-like and C_3 is a saddle point. We denote their positions by the angles $\bar{\alpha}_1$, $\bar{\alpha}_2$ and $\bar{\alpha}_3$ where these angles are measured in the (x, z)-plane from the negative x-axis such that the bottom wing centre-line is at $-180°$ and the top wing centreline is at 180°; see figure 17. These angles are shown plotted versus γ_0 in figure 18, from which it may be seen that at small γ_0, C_1 lies in the

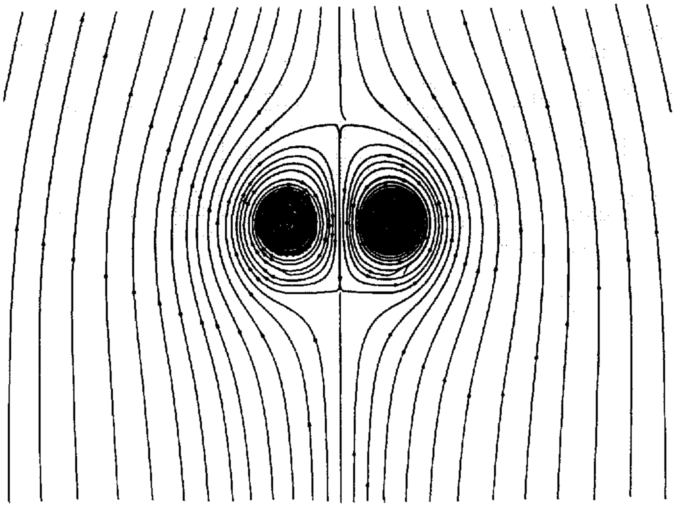

FIGURE 15. Streamlines of the v_θ, v_ψ velocity components on the hemisphere $x > 0$ and viewed along the x-axis, $\gamma_0 = 2.8°$. In addition to the critical points shown there is a source-like star node at $\theta \approx 2.05$, $\psi = -\pi/2$ and a sink-like node at $\theta \approx 1.10$, $\psi = \pi/2$

hemisphere $z < 0$ and C_2, C_3 lie in the hemisphere $z > 0$. Note also that for γ_0 small, $\bar{\alpha}_1 - \bar{\alpha}_3 \approx 180°$. When $\gamma_0 \approx 13°$, C_2 and C_3 approach each other and cancel. The topology then changes to one qualitatively like that shown for $\gamma_0 = 45°$ in figure 16. For this case all of the critical points on the unit sphere are visible. C_1 has moved to $\bar{\alpha}_1 \approx 130.7°$ ($\theta \approx 49.3°$, $\psi = -90°$) and all the streamlines from this node spiral into the vortex-sheet region. For $\gamma_0 = 30°$, C_1 is at $\bar{\alpha}_1 \approx 90°$ ($\theta \approx 90°$, $\psi = -90°$). For some γ_0 in the range 45° to 60°, C_1 'impacts' the wing and there is a transition to a pattern like that shown for $\gamma_0 = 89.5°$ in figure 16 with a 'half-source' on the plane of symmetry at $\theta = 0$, $\psi = 90°$. By comparison, for the strictly two-dimensional attached flow past a semi-infinite flat plate, $\gamma_0 = 90°$ ($n = 0.5$), the flow plotted in this way consists of a 'half-source' on the underside of the wing ($\theta = 0$, $\psi = -90°$) and a 'half-sink' on the top side $\theta = 0$, $\psi = -90°$.

7.4. *The limit* $\gamma_0 \rightarrow 0$; *comparison with slender-body theory*

Figure 19 shows the variation with γ_0 of $1 - n$ and of $y_v = \sin\theta_v \cos\psi_v$, $z_v = \sin\theta_v \sin\psi_v$, the y (lateral) and z (normal to the wing) positions of the line vortex on the unit sphere, plotted as $y_v/\tan\gamma_0$, $z_v/\tan\gamma_0$. When $\gamma_0 \rightarrow 0$, $1 - n$ and $z_v/\tan\gamma_0$ appear to show power-law behaviour, and we find respectively

$$n \approx 1 - 0.319\,\gamma_0^{1.5} \tag{7.3}$$

(γ_0 in radians) which can be compared with the attached-flow result (1.10), and

$$\frac{z_v}{\tan\gamma_0} \approx 0.359\,\gamma_0^{-0.37}. \tag{7.4}$$

Equation (7.4) indicates that the angular extent of separated vortex sheets on the sphere is growing relative to the γ_0 when γ_0 is small; this trend is evident from figure 11. It in part accounts for our difficulty in extending our calculations below $\gamma_0 = 1.3°$.

As we saw in equation (2.9), when γ_0 is small and θ is $O(1)$ the potential of the wing element simplifies to

$$\Phi(\theta, \psi) = B\,P_n^{-1}(-\cos\theta)\,\sin\psi, \tag{7.5}$$

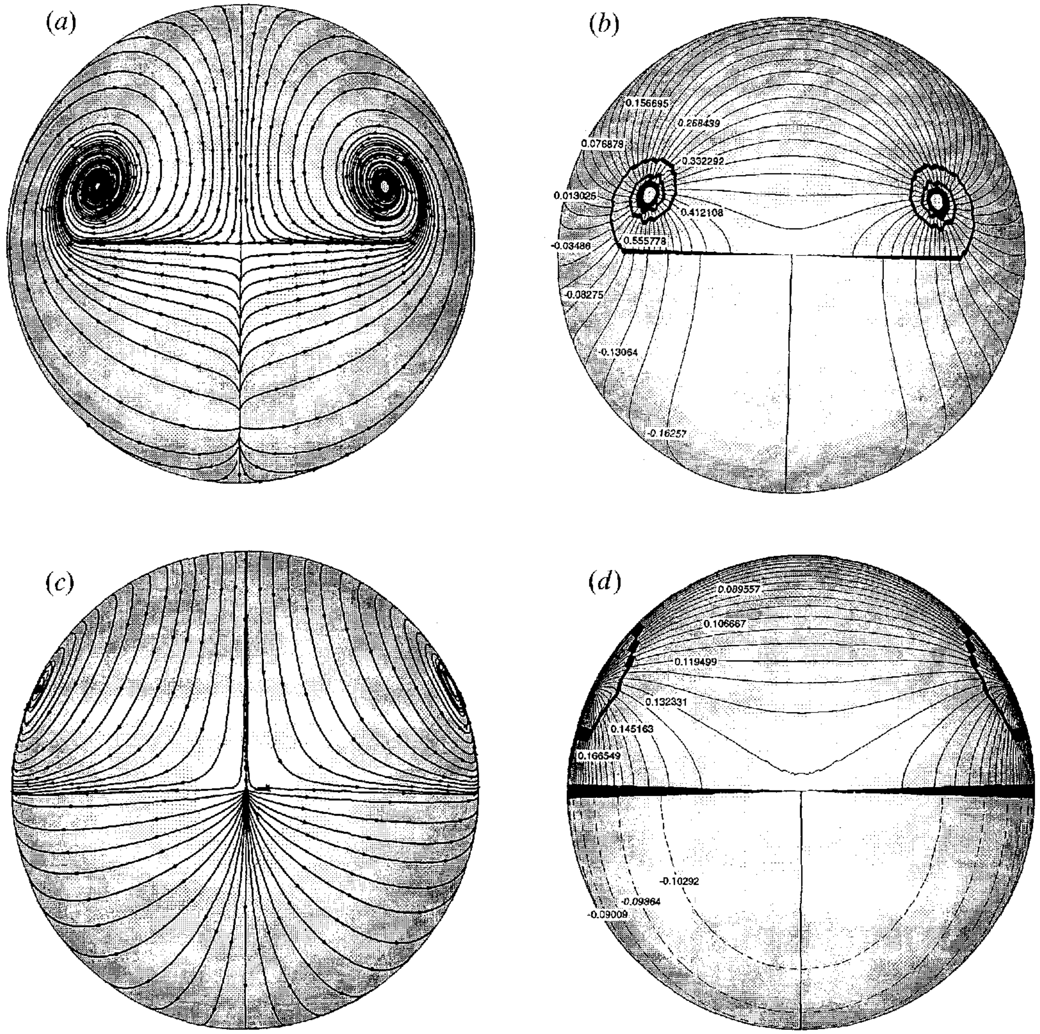

FIGURE 16. (*a*, *c*) v_θ, v_ψ velocity components on the hemisphere $x > 0$ and viewed along the x-axis. (*b*, *d*) Contours of Φ on the same hemisphere. (*a*, *b*) $\gamma_0 = 45°$. (*c*, *d*) $\gamma_0 = 89.5°$. The streamline pattern for $\gamma_0 = 45°$ exhibits a source-like star node at $\theta \approx 0.86$, $\psi = -\pi/2$. There are no critical points on the hemisphere $x < 0$ for either case.

where B is a constant. Our calculations show that $n \to 1$ as $\gamma_0 \to 0$, and thus it is instructive to examine (7.5) in this limit. We write $n = 1 - \epsilon$ and remark that

$$P_{1-\epsilon}^{-1}(-\cos\theta) = {}_2F_1(-1+\epsilon, 2-\epsilon, 2; \omega), \tag{7.6}$$

where $\omega = \cos^2(\frac{1}{2}\theta)$. To obtain the required result we approximate the coefficients in the hypergeometric function expansion to $O(\epsilon)$ and sum the series which results to obtain

$$P_{1-\epsilon}^{-1}(-\cos\theta) = \tfrac{1}{2}\sin\theta + \epsilon A(\omega) + O(\epsilon^2), \tag{7.7}$$

$$A(\omega) = \tfrac{1}{2}\omega - (1-\omega)\log(1-\omega). \tag{7.8}$$

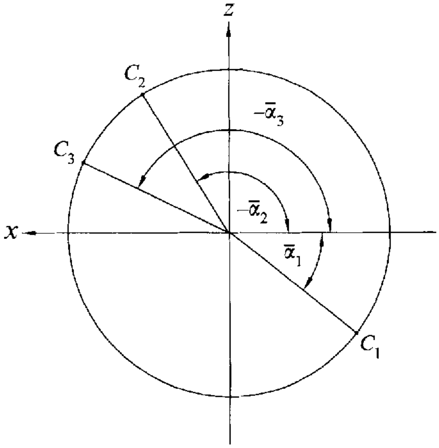

FIGURE 17. Angles $\bar{\alpha}_1$, $\bar{\alpha}_2$ and $\bar{\alpha}_3$ of the critical points C_1, C_2 and C_3 in the (x, z)-plane.

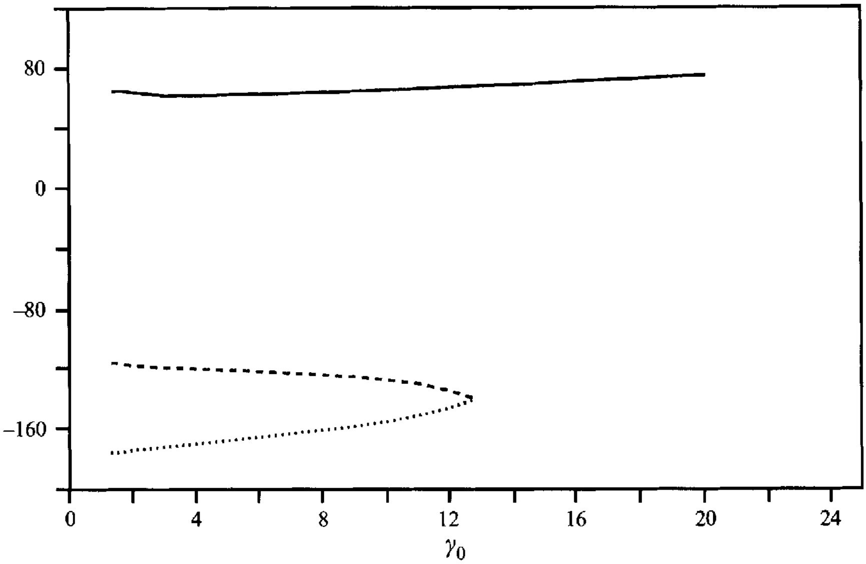

FIGURE 18. Variation of $\bar{\alpha}_1$, $\bar{\alpha}_2$ and $\bar{\alpha}_3$ with γ_0. ———, $\bar{\alpha}_1$; – – – – –, $\bar{\alpha}_2$; ……….., $\bar{\alpha}_3$.

Thus if we fix θ and R and let $\epsilon \to 0$ we have

$$\phi = \tfrac{1}{2} B\, R \sin\psi\, \sin\theta + O(\epsilon), \tag{7.9}$$

or

$$\phi = \tfrac{1}{2} B\, z + O(\epsilon). \tag{7.10}$$

This represents a uniform stream perpendicular to the plane of the winglet. Equation (7.10) shows that as $\gamma_0 \to 0$ so that $n \to 1$, the eigenfunction for the attached flow at any fixed point resembles a uniform stream at an angle of incidence 90°. We stress the non-uniform nature of the limit. For any fixed $\epsilon \ll 1$ the expansion fails as $\theta \to 0$ or as $R \to 0$ or $R \to \infty$.

It is straightforward to show that a uniform stream like the leading-order term of (7.10), when projected onto a (v_θ, v_ψ) field on the unit sphere, produces source/sink critical points at $\theta = 90°, \psi = \pm 90°$. In terms of the discussion of §7.3 these are equivalent, for the attached flow, to the critical points C_1 and C_2. Our solutions to

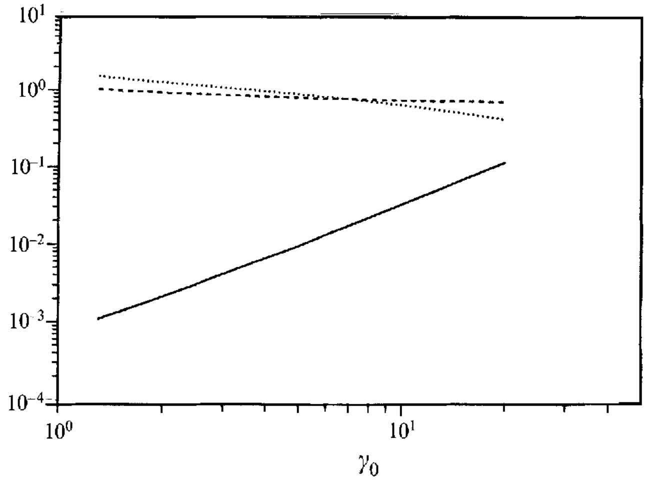

FIGURE 19. Variation of $(1-n)$, $y_v/\tan\gamma_0$ and $x_v/\tan\gamma_0$ with γ_0. ————, $(1-n)$; – – – – –, $y_v/\tan\gamma_0$; ………, $x_v/\tan\gamma_0$.

the separated-flow problem for small γ_0 will have a far field which is that of an equivalent winglet plus the separated vortex sheets, and will thus approximate to a uniform stream at an effective angle of incidence. It was noted in §7.3 that when $\gamma_0 \to 0$, the difference $\bar{\alpha}_1 - \bar{\alpha}_3 \approx 180°$, i.e. the C_1 and C_3 source/sink critical points are antipodal. This suggests that the line joining these critical points forms the direction of an effective free stream which has been 'manufactured' by the eigenfunction, like (7.7) for the attached flow. We therefore take this effective angle of incidence to be $\bar{\alpha}_1$, the angular position of C_1 defined in §7.3. This in turn suggests a comparison with the results of slender-body theory based on $\bar{\alpha}_1$.

For flow with separation modelled by vortex sheets, the slender-body theory gives predictions, when α_0, γ_0 are small, of y_v/γ_0 and x_v/γ_0 as a function of α_0/γ_0, where α_0 is the incidence angle (see Smith 1968). Table 7 shows comparison with the slender-body calculations of Pullin (1973), for small γ_0, using $\sin\bar{\alpha}_1/\tan\gamma_0$ as the independent parameter (we take $\alpha_0 = \bar{\alpha}_1$). These calculations used only one turn of the vortex sheet compared with three turns in the present results and this may account for some of the discrepancies. The trends with increasing $\sin\bar{\alpha}_1/\tan\gamma_0$ are qualitatively similar for both models. We remark that the range of $\sin\bar{\alpha}_1/\tan\gamma_0$ shown is larger than values in typical experiments, and so no experimental data are displayed. Note that we have used $\bar{\alpha}_1$ as the effective angle of attack even for $\gamma_0 > 13°$, where the C_2 critical point has vanished. We have been unable to make comparisons with slender-body theory for γ_0 less than 9° because results for slender-body theory at sufficiently large $\sin\bar{\alpha}_1/\tan\gamma_0$ do not appear to be available. Figure 18 indicates that when $\gamma_0 \to 0$, $\bar{\alpha}_1 \to 64°$ approximately compared to an effective angle of incidence of 90° for the attached flow implied by (7.10). The reason for this discrepancy is the apparent tendency $x_v \tan\gamma_0 \to \infty$ when $\gamma_0 \to 0$ suggested by (7.3). This means that the angular extent of the vortex sheets are growing relative to γ_0 and so the wing plus the vortex sheets cannot then be accurately approximated by (7.5)

Finally, in Figures 20–22 are shown the lines of three vector fields on the half-wing $y > 0$ and on the first half-turn of the vortex sheet. The vortex lines, shown as plot (c) in each figure are everywhere orthogonal to the vector field which is the three-dimensional velocity difference across the surface of discontinuity. In each case the vortex lines show rapid directional changes near the wing edge and appear to

γ_0 (deg.)	$\bar{\alpha}_1$ (deg.)	$\dfrac{\sin\bar{\alpha}_1}{\tan\gamma_0}$	$\dfrac{y_v}{\tan\gamma_0}$ present	$\dfrac{y_v}{\tan\gamma_0}$ slender body	$\dfrac{z_v}{\tan\gamma_0}$ present	$\dfrac{z_v}{\tan\gamma_0}$ slender body
9	63.5	5.66	0.7756	0.695	0.7017	0.700
10	64.3	5.11	0.7707	0.680	0.6666	0.680
11	65.0	4.66	0.7676	0.675	0.6351	0.660
12	66.0	4.30	0.7643	0.670	0.6067	0.635
13	66.8	3.98	0.7624	0.667	0.5807	0.615
14	67.5	3.71	0.7609	0.669	0.5569	0.595
15	68.5	3.47	0.7598	0.671	0.5349	0.575
16	69.8	3.27	0.7590	0.672	0.5145	0.555
17	70.7	3.09	0.7582	0.673	0.4955	0.545
18	71.8	2.93	0.7576	0.674	0.4779	0.530
19	72.9	2.67	0.7567	0.675	0.4614	0.515
20	74.0	2.64	0.7557	0.677	0.4460	0.505

TABLE 7. Comparison of the y- and z-positions of the isolated vortex compared with calculations (Pullin 1973) based on slender-body theory.

leave the wing nearly normal to this edge. This direction would be exactly normal if $\mathrm{d}f/\mathrm{d}\sigma = 0$ right at the edge rather than just inboard of the edge.

8. Concluding remarks

The present model, quite apart from features of real delta-wing flows such as secondary separation, is likely to be valid only on the forward part of the wing very near the apex. There is no way to determine the fraction of the maximum chord L in which our solution holds short of solving the full inviscid problem for the finite delta wing at incidence. Mathematically, our solution should supply a boundary condition to remove the near-apex singularity for this calculation. The case of a slender finite delta is special, because, as we have seen, our eigenfunction tends to a solution of the slender-body equations as $\gamma_0 \to 0$. However, as our results show, there is a mismatch between the angular positions of the vortices as given by our theory and the angular positions given by slender-body theory for small angles of incidence. This means that slender-body theory will give increasingly poor results as $x/L \to 0$ for small fixed γ_0. On the other hand, for fixed $x/L < 1$, we expect the slender-body theory solution to hold in the limit $\gamma_0 \to 0$. We know of no established experimental data on the vortex locations over, say, the leading 25% of the wing centreline chord which may be able to test the predictions of the slender-body theory versus the present calculations. We hope that the present work will stimulate such experiments.

Our present numerical methods, both Scheme A and Scheme B, use a simple linear-element representation of the separated vortex sheet and a lumped, single-element model of the innerportion. It is clear from the local solution given in Appendix C that there are non-analyticities present in the solution at the edge. Attempts to build these into the numerical schemes on the wing side have been made here, but no comparable method has been developed for handling the first few elements of the free vortex sheet and, in particular, the pressure continuity condition at the separation point. The crudeness of this numerical approach can be seen from the way in which the local identities of table 5 and the continuity of $\mathrm{d}f/\mathrm{d}\sigma$ at the edge, shown in table 6, are satisfied only approximately. The development of a more accurate representation of the vortex sheet which incorporates continuity of at least the first derivative at

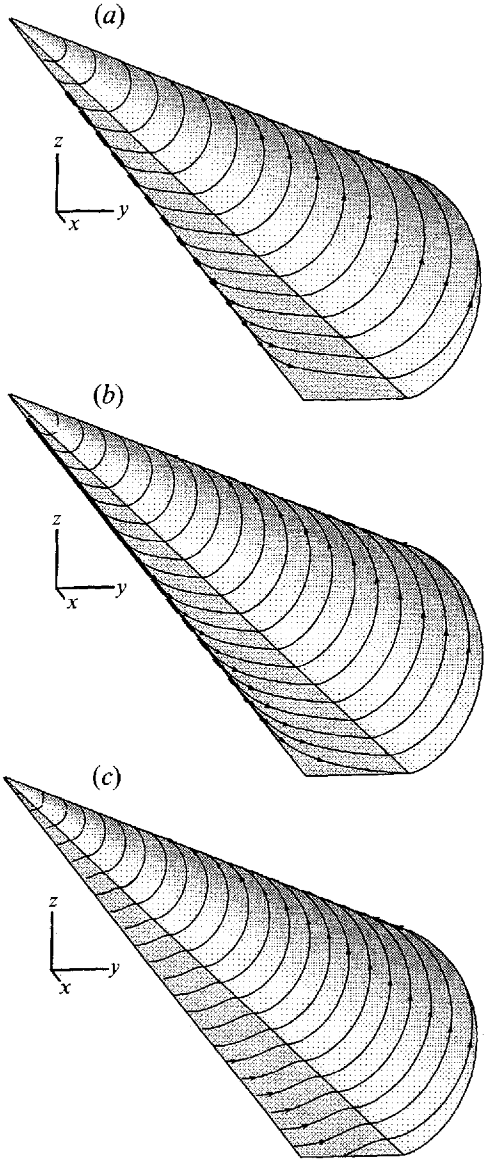

FIGURE 20. Lines of three vector fields on a surface consisting of the half-wing $y > 0$ and the first half-turn of the separated vortex sheet, $\gamma_0 = 2.8°$. (*a*) Streamlines of the upper ($z = 0^+$) wing surface and the corresponding side of the separated sheet. (*b*) Streamlines of the lower ($z = 0^-$) wing surface and the corresponding side of the separated sheet. (*c*) vortex lines.

the nodes, the explicit inclusion of the non-analyticities on the sheet side into the numerical method, and an improved way of treating the inner rolled-up portion of the sheet, remain challenges for future work.

This research was supported partly by the SERC of the United Kingdom under grant number GR/J02179, the National Science Foundation of the USA under Grant no CTS-9311811 and the Department of Energy of the USA under Grant No. DE-FG03-89ER25073.

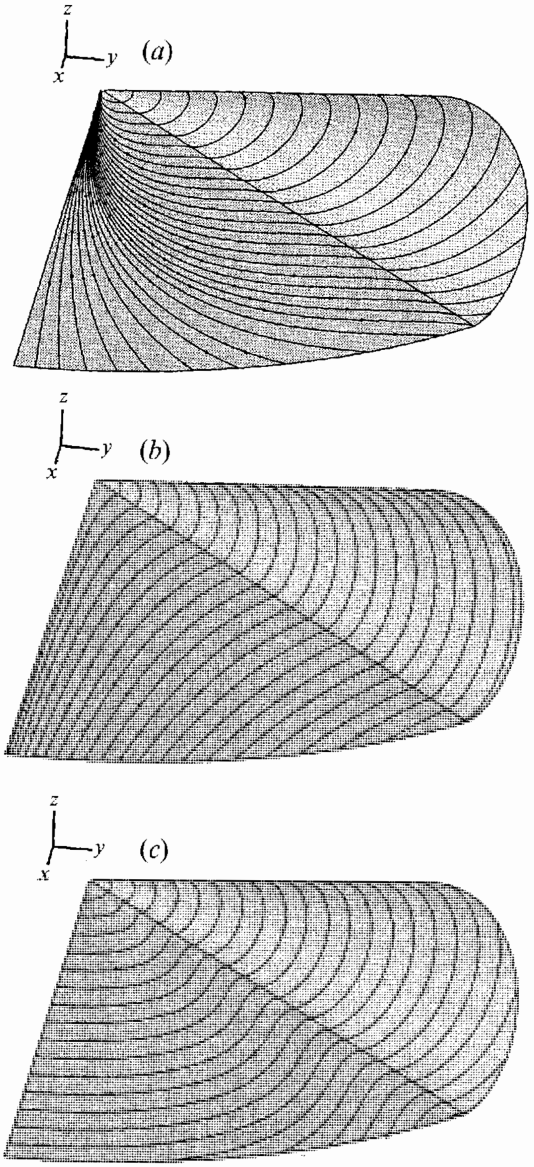

FIGURE 21. As figure 20 but for $\gamma_0 = 45°$.

Appendix A. Geometry of the sheet element

We must explain how we obtain the basic variables $(\alpha_1, \alpha_2, \rho_1, \rho_2)$ defining the element E in terms of (θ_1, ψ_1) and (θ_2, ψ_2), the spherical polar coordinates of its extremities.

Using (4.1), (4.3), and (4.4), we have

$$\cos\theta_1 = \cos\alpha_1 \cos\rho_1 - \sin\alpha_1 \cos\alpha_3 \sin\rho_1, \tag{A 1}$$

$$\sin\theta_1 \cos\psi_1 = \sin\alpha_1 \cos\rho_1 + \cos\alpha_1 \cos\alpha_3 \sin\rho_1, \tag{A 2}$$

$$\sin\theta_1 \sin\psi_1 = \sin\alpha_3 \sin\rho_1; \tag{A 3}$$

the same equations hold with $(\theta_1, \psi_1) \to (\theta_2, \psi_2)$ and $\rho_1 \to \rho_2$.

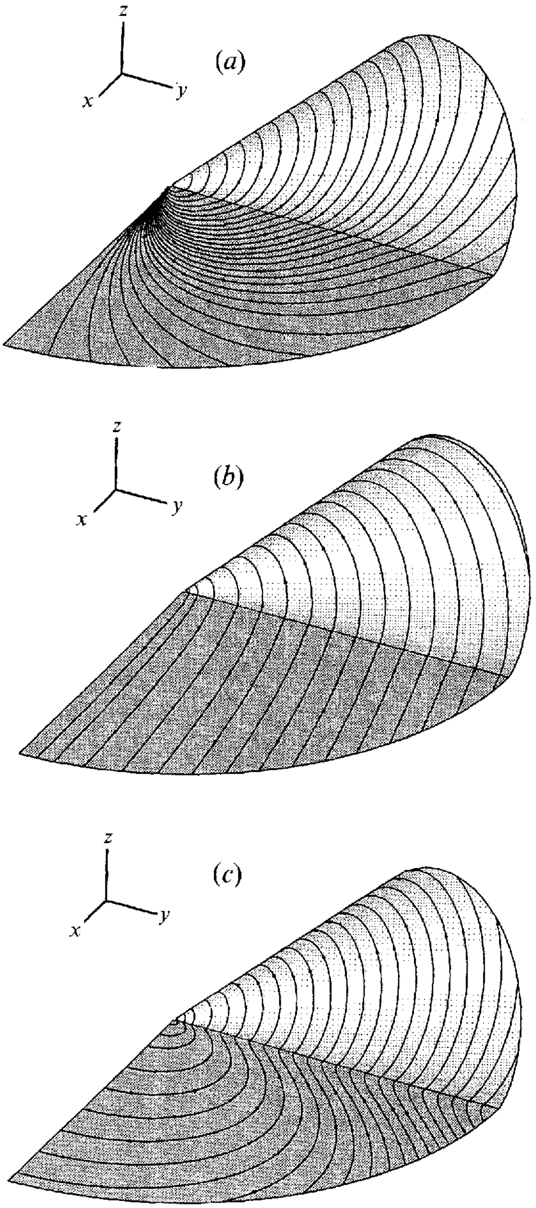

FIGURE 22. As figure 20 but for $\gamma_0 = 89.5°$.

Solving the linear equations (A1) and (A2) for $\cos\rho_1$ and $\sin\rho_1$, we find

$$\sin\rho_1 = \frac{\sec\alpha_3}{(-\sin\alpha_1\cos\theta_1 + \cos\alpha_1\sin\theta_1\cos\psi_1)}, \tag{A 4}$$

and using (A3) gives

$$\tan\alpha_3 = \frac{\sin\theta_1\sin\psi_1}{(-\sin\alpha_1\cos\theta_1 + \cos\alpha_1\sin\theta_1\cos\psi_1)}. \tag{A 5}$$

Similarly

$$\tan\alpha_3 = \frac{\sin\theta_2 \sin\psi_2}{(-\sin\alpha_1\cos\theta_2 + \cos\alpha_1 \sin\theta_2 \cos\psi_2)}. \tag{A 6}$$

If we eliminate $\tan\alpha_3$ between (A5) and (A6) we obtain

$$\tan\alpha_1 = \frac{\sin\theta_1 \sin\theta_2 \sin(\psi_1 - \psi_2)}{(\cos\theta_2 \sin\theta_1 \sin\psi_1 - \cos\theta_1 \sin\theta_2 \sin\psi_2)}. \tag{A 7}$$

If we require $-\pi/2 < \alpha_1 < \pi/2$, (A7) fixes α_1 uniquely.

We can now obtain α_3 from (A6), making α_3 unique by insisting that $0 \leqslant \alpha_3 \leqslant \pi$. To ensure the correct branch of α_1 is used, we write (A7) as

$$\alpha_1 = \mathrm{atan2}\,(s_1, s_2),$$

where $s_1 = \sin\theta_1 \sin\theta_2 \sin(\psi_1 - \psi_2)$ and $s_2 = \sin\theta_1 \sin\psi_1 \cos\theta_2 - \cos\theta_1 \sin\theta_2 \sin\psi_2$ and where atan2(*, *) is the standard FORTRAN library function. This ensures that $\hat{\boldsymbol{n}}$ varies continuously.

Appendix B. Vortex force on the central terminal sheet element

In this Appendix we show how (5.8), applied to the terminal element E_M, can be used to derive the boundary condition for this element. We choose a control volume V whose projection on the unit sphere is in the form of a 'keyhole' surrounding E_M and crossing at the join of E_M and E_{M-1} and whose radial extent is ΔR; see figure 5. Since H is constant away from E_M and is bounded in the sheet, the integral on the right-hand side of (5.8) vanishes. Thus the net vortex force vanishes.

To derive the boundary condition, we have to evaluate the integral on the left-hand side of (5.8). We choose local axes such that $z = y = 0$ corresponds to the right-hand extremity of E_M (see figure 5) and introduce local polar coordinates by $x = \rho\cos\chi$ and $y = \rho\sin\chi$ where in this Appendix, ρ is a local radius. In these coordinates E_M corresponds to $-\gamma \leqslant \chi \leqslant 0$, $z = 0$, where γ is the angular extent of the element and the vorticity is given, in the same angular range by

$$\omega = g_{M-1}\left(R^n\delta(y)\delta(z)\hat{\boldsymbol{i}} + nR^{n-1}\delta(z)\hat{\underline{\chi}}\right), \tag{B 1}$$

where δ here represents the delta function. Equation (B1) follows directly from the construction of §2. We thus have

$$\int_{V_1} \omega \wedge \boldsymbol{u}\,\mathrm{d}V = \boldsymbol{I}_1 + \boldsymbol{I}_2, \tag{B 2}$$

where

$$\boldsymbol{I}_1 = g_{M-1}\,\mathrm{d}R \iint_{A_1} \delta(y)\delta(z)\left(\hat{\boldsymbol{i}} \wedge \boldsymbol{u}\right)\,\mathrm{d}y\,\mathrm{d}z, \tag{B 3}$$

and

$$\boldsymbol{I}_2 = g_{M-1}\,n\,\mathrm{d}R \iint_{A_2} \delta(z)\left(\hat{\underline{\chi}} \wedge \boldsymbol{u}\right)\mathrm{d}\theta\,\mathrm{d}z. \tag{B 4}$$

We consider the integral $\boldsymbol{I}_1$ first. In the neighbourhood of A the velocity field is the sum of two contributions. There is a point vortex of strength g_{M-1} and a uniform flow $\hat{\boldsymbol{i}}U_E + \hat{\boldsymbol{j}}V_E + \hat{\boldsymbol{k}}W_E$, which is the sum of contributions from the wing, the elements

$\underline{E}_1, \underline{E}_2, \cdots, \underline{E}_M$ as defined in §5.1, the elements $E_1, E_2, \cdots, E_{M-1}$ and the self-induced velocity of E_M – this is finite, since the element E_M has uniform winglet strength and the logarithmic term is absent.

The point vortex makes no contribution to $\boldsymbol{I}_1$, which thus reduces to

$$\boldsymbol{I}_1 = \mathrm{d}R\, g_{M-1}\left(-\hat{\boldsymbol{j}} W_E + \hat{\boldsymbol{k}} V_E\right); \tag{B 5}$$

this is equivalent to the Kutta lift on the edge vortex.

On evaluating the vector product, $\boldsymbol{I}_2$ reduces to

$$\boldsymbol{I}_2 = \mathrm{d}R\, n\, g_{M-1} \int_{-\Delta_2}^{\Delta_2}\int_{-\gamma}^{0} \left(\hat{\boldsymbol{i}} w \cos\chi + \hat{\boldsymbol{j}} w \sin\chi - \hat{\boldsymbol{k}} U_R\right) \mathrm{d}\chi\, \mathrm{d}z, \tag{B 6}$$

where U_R is the radial component of the velocity. But

$$U_R = n R^{n-1}\, \Phi = n\left(\Phi_e + \tfrac{1}{2} g_{M-1} \mathrm{sign}(z)\right). \tag{B 7}$$

Thus

$$\boldsymbol{I}_2 = \mathrm{d}R\, n\, g_{M-1} \int_{-\gamma}^{0} \left(\hat{\boldsymbol{i}} w \cos\chi + \hat{\boldsymbol{j}} w \sin\chi - n \hat{\boldsymbol{k}} \Phi_e\right) \mathrm{d}\chi \tag{B 8}$$

and on extracting the $\hat{\boldsymbol{j}}$- and $\hat{\boldsymbol{k}}$-components, we find that

$$-W_E + n \int_{-\gamma}^{0} w \sin\chi \mathrm{d}\chi = 0, \tag{B 9}$$

and

$$V_E - n^2 \int_{-\gamma}^{0} \Phi_e \mathrm{d}\chi = 0. \tag{B 10}$$

Now

$$w \sim \frac{g_{M-1}}{2\pi\chi} \quad \text{as} \quad \chi \to 0- \quad , \tag{B 11}$$

so the integral in (B9) is convergent. However the $\hat{\boldsymbol{i}}$-component is infinite, due essentially to the infinite pressure on the axis of the tightly rolled portion of the sheet. This infinity can only be removed by viscosity, but we will not pursue this here.

Finally, we approximate (B9) and (B10) for $\gamma \to 0$ and we find that

$$-W_E + \frac{n\, g_{M-1}}{2\pi}\gamma = 0, \tag{B 12}$$

and

$$V_E - n^2 \gamma \Phi_e(0) = 0. \tag{B 13}$$

This approximation is consistent, since we expect the element E_M to shrink as the resolution is increased.

Appendix C. Local solution near wing edge

We seek a leading-order local solution to (1.6) valid close to the wing tip, and use local spherical coordinates $\bar{\theta}, \bar{\psi}$ with the polar axis $\bar{\theta} = 0$ along the wing edge The upper/lower wing surfaces are defined by $\bar{\psi} = \pi$, $\bar{\psi} = -\pi$ respectively. Let the shape of the separating vortex sheet be

$$\bar{\psi} = F(\bar{\theta}). \tag{C1}$$

The boundary conditions on the wing are

$$\frac{\partial \Phi}{\partial \bar{\psi}} = 0, \qquad \bar{\psi} = \pm\pi. \tag{C2}$$

The kinematic and dynamic (pressure) conditions on the separating sheet are

$$\frac{1}{\sin^2\bar{\theta}}\frac{\partial \Phi}{\partial \bar{\psi}} = \frac{\partial F}{\partial \bar{\theta}}\frac{\partial \Phi}{\partial \bar{\theta}}, \tag{C3}$$

$$n^2\Phi_+^2 + \left(\frac{\partial \Phi_+}{\partial \bar{\theta}}\right)^2 + \frac{1}{\sin^2\bar{\theta}}\left(\frac{\partial \Phi_+}{\partial \bar{\psi}}\right)^2 = n^2\Phi_-^2 + \left(\frac{\partial \Phi_-}{\partial \bar{\theta}}\right)^2 + \frac{1}{\sin^2\bar{\theta}}\left(\frac{\partial \Phi_-}{\partial \bar{\psi}}\right)^2 \tag{C4}$$

on $\bar{\psi} = F(\bar{\theta})$. Upon making the transformation $x = \cos\bar{\theta}$, $\Phi = \exp(\mathrm{i}m\bar{\psi})\,\bar{\Phi}$ in (1.6), this equation becomes

$$\frac{\mathrm{d}}{\mathrm{d}x}\left((1-x^2)\frac{\mathrm{d}\bar{\Phi}}{\mathrm{d}x}\right) - \frac{m^2}{1-x^2}\bar{\Phi} + n(n+1)\,\bar{\Phi} = 0, \tag{C5}$$

the solution of which may be written as

$$\bar{\Phi} = \frac{1}{\Gamma(1+m)}\tan^m(\tfrac{1}{2}\bar{\theta})\,{}_2F_1\left(-a,b,c,\sin^2(\tfrac{1}{2}\bar{\theta})\right), \tag{C6}$$

where $a = n$, $b = n+1$, $c = m+1$, $\Gamma(..)$ denotes the gamma function and ${}_2F_1$ is the hypergeometric function.

To obtain solutions for $\bar{\Phi}_+$ and $\bar{\Phi}_-$ above and below the wing respectively, we take linear combinations of the solutions for $m = 0$, 1, $\frac{3}{2}$, 2, (omiting $m = \frac{1}{2}$ since this gives singular velocities at the tip), and retain terms in the expansion of the right-hand side of (C6) to $O(\bar{\theta}^2)$. This gives

$$\Phi_+ = A_+\left(1 + \tfrac{ab}{4c}\,\bar{\theta}^2 + \cdots\right) + U_+\,\bar{\theta}\,\cos\bar{\psi} + \alpha_+\,\bar{\theta}^{3/2}\sin\left(\tfrac{3}{2}\bar{\psi}\right) + D_+\,\bar{\theta}^2\,\cos 2\bar{\psi}, \tag{C7}$$

$$\Phi_- = A_-\left(1 + \tfrac{ab}{4c}\,\bar{\theta}^2 + \cdots\right) + U_-\,\bar{\theta}\,\cos\bar{\psi} + \alpha_-\,\bar{\theta}^{3/2}\sin\left(\tfrac{3}{2}\bar{\psi}\right) + D_-\,\bar{\theta}^2\,\cos 2\bar{\psi}, \tag{C8}$$

where $A_\pm$, $U_\pm$, $\alpha_\pm$ and $D_\pm$ are constants. It may be seen that (C7)–(C8) satisfies (C2) by construction. Applying (C3) on each side of the separated sheet gives

$$\frac{\mathrm{d}F}{\mathrm{d}\bar{\theta}} = \frac{-U_\pm\bar{\theta}\,\sin F + \frac{3}{2}\alpha_\pm\bar{\theta}^{3/2}\,\cos(\frac{3}{2}F) - 2\,D_\pm\,\bar{\theta}^2\,\sin 2\bar{\psi}\cdots}{\bar{\theta}^2\,\left(U_\pm\cos F + \frac{3}{2}\,\alpha_\pm\bar{\theta}^{1/2}\sin(\frac{3}{2}F) + O(\bar{\theta})\right)}. \tag{C9}$$

Now assume

$$F = C_\pm\,\bar{\theta}^{1/2} + \cdots, \qquad C_+ = C_-. \tag{C10}$$

Then from (C9)

$$C_\pm = \frac{-2\,U_\pm\,C_\pm + 3\,\alpha_\pm}{U_\pm}, \tag{C11}$$

and consequently

$$C_+ = \frac{\alpha_+}{U_+} = C_- = \frac{\alpha_-}{U_-}. \tag{C12}$$

It may be verified that when the above is used in (C7)–(C8), the pressure condition

(C4) is satisfied to leading order. The separated sheet shape is then given by

$$\bar{\psi} = C_{\pm}\bar{\theta}^{1/2} = \frac{\alpha_{\pm}}{U_{\pm}}\bar{\theta}^{1/2}. \tag{C 13}$$

Thus the shape of the separating sheet and $\bar{\Phi}_{\pm}$ are related by (C11) which we will refer to as the *local identities*. The constants $U_{\pm}$ and $\alpha_{\pm}$ cannot, however, be determined by the local analysis but must be calculated as part of the global solution. Transforming from $(\bar{\theta},\bar{\psi})$ to global (θ,ψ) coordinates gives for the shape

$$\psi = \frac{C_{\pm}}{\sin\gamma_0}(\theta-\gamma_0)^{3/2}+\cdots. \tag{C 14}$$

while the winglet strength $f = \bar{\Phi}_{+}-\bar{\Phi}_{-}$ is, from (C7)–(C8)

$$f(\theta) = A_{+}-A_{-}+(U_{-}-U_{+})(\gamma_0-\theta)-(\alpha_{+}+\alpha_{-})(\gamma_0-\theta)^{3/2}\cdots. \tag{C 15}$$

Appendix D. Asymptotics of the rolled-up sheet

We wish to describe the inner portion of the separated vortex sheet, and again employ local spherical coordinates $R,\bar{\theta},\bar{\psi}$ with, in this case, the polar axis $\bar{\theta}=0$ along the axis of roll-up and the azimuthal angle $\bar{\psi}$ measured from an arbitrary plane which contains this axis. We seek a solution of the equations of motion in which all components of the velocity $(v_R, v_{\bar{\theta}}, v_{\bar{\psi}})$ are independent of $\bar{\psi}$. This allows the definition of a stream function Ψ and a vorticity Ω, in terms of which the velocity components may be written

$$v_R = \frac{1}{R^2\sin\bar{\theta}}\frac{\partial\Psi}{\partial\bar{\theta}} \qquad v_{\bar{\theta}} = -\frac{1}{R\sin\bar{\theta}}\frac{\partial\Psi}{\partial R} \qquad v_{\bar{\psi}} = \frac{\Omega}{R\sin\bar{\theta}}\ . \tag{D 1}$$

The Navier–Stokes equations motion are then (see Goldstein 1965, p. 114)

$$\frac{2\,\Omega}{R^2\sin^2\bar{\theta}}\left(\frac{\partial\Omega}{\partial R}\cos\bar{\theta}-\frac{1}{R}\frac{\partial\Omega}{\partial\bar{\theta}}\sin\bar{\theta}\right)-\frac{1}{R^2\sin\bar{\theta}}\frac{\partial(\Psi,\mathrm{D}^2\Psi)}{\partial(R,\bar{\theta})}$$
$$+\frac{2\,\mathrm{D}^2\Psi}{R^2\sin^2\bar{\theta}}\left(\frac{\partial\Psi}{\partial R}\cos\bar{\theta}-\frac{1}{R}\frac{\partial\Psi}{\partial\bar{\theta}}\sin\bar{\theta}\right) = \nu\,\mathrm{D}^4\Psi, \tag{D 2}$$

$$\frac{1}{R^2\sin\bar{\theta}}\frac{\partial(\Psi,\Omega)}{\partial(R,\bar{\theta})} = \nu\,\mathrm{D}^2\Omega, \tag{D 3}$$

$$\mathrm{D}^2 = \frac{\partial^2}{\partial R^2}+\frac{\sin\bar{\theta}}{R^2}\frac{\partial}{\partial\bar{\theta}}\left(\frac{1}{\sin\bar{\theta}}\frac{\partial}{\partial\bar{\theta}}\right). \tag{D 4}$$

where ν is the kinematic viscosity.

We seek a solution of the form

$$\Psi = R^{n+1}\,\hat{\Psi}(\bar{\theta}), \qquad \Omega = R^n\,\hat{\Omega}, \tag{D 5}$$

and for inviscid flow, $\nu=0$, (D3) then becomes

$$(n+1)\,\hat{\Psi}\,\frac{\partial\hat{\Omega}}{\partial\bar{\theta}}-n\,\hat{\Omega}\,\frac{\partial\hat{\Psi}}{\partial\bar{\theta}} = 0. \tag{D 6}$$

Now assume that for $\bar{\theta}$ small, $\hat{\Psi}$ and $\hat{\Omega}$ have the form

$$\hat{\Psi} = A_1\,\bar{\theta}^{\mu_1}, \qquad \hat{\Omega} = A_2\,\bar{\theta}^{\mu_2}, \tag{D 7}$$

where A_1, A_2 are constants and μ_1, μ_2 exponents to be determined. Equation (C6) gives

$$(n+1)\mu_2 - n\mu_1 = 0. \tag{D 8}$$

Substitution of (D7) into (D2), expansion in powers of $\bar{\theta}$, and the use of a dominant balance argument gives $\mu_1 = n+1$; $\mu_2 = n$ then follows from (D8). The velocity components are thus given by, for small $\bar{\theta}$,

$$\left.\begin{aligned} v_R &= A_1(n+1)R^{n-1}\bar{\theta}^{\,n-1}, \\ v_{\bar{\theta}} &= -A_1(n+1)R^{n-1}\bar{\theta}^{\,n}, \\ v_{\bar{\varphi}} &= -A_2(n+1)R^{n-1}\bar{\theta}^{\,n-1}. \end{aligned}\right\} \tag{D 9}$$

Use of $v_{\bar{\theta}}$ and $v_{\bar{\varphi}}$ in the kinematic condition (C3) then shows that when $\bar{\varphi}$ is large, the rolled-up, conical-spiral vortex sheet is of the form

$$r = R\bar{\theta} \sim \bar{\varphi}^{-1}. \tag{D 10}$$

Its asymptotic shape is thus independent of the similarity exponent n. The above may be used as a starting point for the analysis of viscous effects in the rolled-up core.

REFERENCES

ABRAMOWITZ, A. & STEGUN, I. S. 1964 *Handbook of Mathematical Functions.* National Bureau of Standards.

BROWN, C. E. & MICHAEL, W. H. 1959 On slender delta wings with leading-edge separation. *Proc. R. Soc. Lond.* A **251**, 200–217.

BROWN, S. N. & STEWARTSON, K. 1969 Flow near the apex of a plane delta wing. *J. Inst. Maths Applics.* **5**, 206–216 (referred to herein as BS).

GLAUERT, H. 1946 *The Elements of Aerofoil and Airscrew Theory.* Cambridge University Press.

GOLDSTEIN, S. (Ed.) 1965 *Modern Developments in Fluid Dynamics,* Vol 1. Dover.

GUDERLY, G. 1942 Starke kugelige und zylinderische Verdichtungstoesse in der Naehe des Kugelmittepunktes bzw der Zylinderachse. *Luftfahrtforschung* **19**, 302–312.

KIRKKOPRU, K. & RILEY, N. 1991 Secondary separation from a slender wing. *J. Engng Maths* **25**, 329–352.

KUCHEMANN, D. 1975 *The Aerodynamic Design of Aircraft.* Pergamon.

MAGNUS, W. & OBERHETTINGER, F. 1954 *Formulas and Theorems for the Functions of Mathematical Physics.* Chelsea.

PULLIN, D. I. 1973 A method for calculating inviscid separated flow about conical slender bodies. *Aeronautical Research Laboratories (Australia) Aero. Rep.* 238.

PULLIN, D. I. 1978 The large-scale structure of self-similar rolled-up vortex sheets. *J. Fluid Mech.* **88**, 401–430.

RILEY, N. & SMITH, J. H. B. 1985 Prediction of leading-edge vortex behaviour to supplement the suction analogy. *J. Engng Maths* **19**, 157–192.

SMITH, J. H. B. 1968 Improved calculations of leading-edge separation from slender delta wings. *Proc R. Soc. Lond.* A **306**, 67–90.

THOMPSON, D. H. 1975 A water tunnel study of vortex breakdown over wings with highly swept leading edges. *Aeronautical Research Laboratories (Australia) Aero. Note* 356. See also *ARL Aero. Note* 338 (1973).

VAN DER VOOREN, A. I. 1980 A numerical investigation of the rolling up of vortex sheets. *Proc. R. Soc. Lond.* A 373, 67–92.